Geochronological evolution of the potentially active Iliniza Volcano (Ecuador) based on new K-Ar ages

Santiago Santamaria, Xavier Quidelleur, Silvana Hidalgo, Pablo Samaniego, Jean-Luc Le Pennec, Céline Liorzou, Pierre Lahitte, Marco Córdova, Pedro Espín

Santiago Santamaria, Xavier Quidelleur, Silvana Hidalgo, Pablo Samaniego, Jean-Luc Le Pennec, et al.. Geochronological evolution of the potentially active Iliniza Volcano (Ecuador) based on new K-Ar ages. Journal of Volcanology and Geothermal Research, 2022, pp.107489. 10.1016/j.jvolgeores.2022.107489 . hal-03553857

HAL Id: hal-03553857
https://uca.hal.science/hal-03553857

Submitted on 3 Feb 2022

Geochronological evolution of the potentially active Iliniza Volcano (Ecuador) based on new K-Ar ages

Santiago Santamaria [a]*, Xavier Quidelleur [a], Silvana Hidalgo [b], Pablo Samaniego [c], Jean-Luc Le Pennec [d, e], Céline Liorzou [d], Pierre Lahitte [a], Marco Córdova [b], Pedro Espín [b]

[a] GEOPS, Université Paris-Saclay, CNRS, Rue du Belvédère, 91405 Orsay, France

[b] Instituto Geofísico, Escuela Politécnica Nacional, Ap. 17-01-2759, Quito, Ecuador

[c] Laboratoire Magmas et Volcans, Université Clermont Auvergne, CNRS, IRD, OPGC, F-63000 Clermont-Ferrand, France

[d] Geo-Ocean, Institut Universitaire Européen de la Mer, Université de Bretagne Occidentale, CNRS-UBO-Ifremer-UBS, Rue Dumont d'Urville, 29280 Plouzané, France

[e] IRD – Délégation Ouest, Technopôle Brest-Iroise, CS10070, 29280 Plouzané, France

*Corresponding author. santiago.santamaria@universite-paris-saclay.fr, sdsantiago@gmail.com

Keywords:

- Iliniza volcano
- Ecuador
- K-Ar dating
- Geomorphology
- Volcanic hazards

Highlights:

- Iliniza volcano is formed by two late-Pleistocene edifices and their satellite vents.
- The North Iliniza edifice started growing at ~123 ka and ended at ~116 ka.
- The South Iliniza edifice was built from ~46 to ~25 ka and produced a VEI 5 event.
- Effusive eruptions took place during the Holocene from 2 southern satellite vents.
- Iliniza volcano should be considered as a potentially active volcano.

ABSTRACT

The youngest volcanism of the Ecuadorian Volcanic Front (Western Cordillera) is mainly dominated by highly explosive events, including the growth and violent destruction of lava domes, and the formation of thick pyroclastic sequences. Deposits associated with such eruptive dynamics have been identified at Iliniza, a compound volcano located in the Western Cordillera with a poorly defined evolutionary history. We present the first K-Ar ages of Iliniza volcano combined with stratigraphic data, numerical reconstructions, and geochemical analyses, providing a new perspective on its evolution. Our results show that Iliniza volcano is much younger than previously proposed. The Iliniza twin-peaked shape is the result of the superposition of two andesitic to dacitic stratovolcanoes. (1) The North Iliniza (NI) edifice was constructed by two lava successions and an intermediate satellite vent, showing a short range of mainly effusive activity between 123 ± 6 and 116 ± 2 ka. (2) The South Iliniza (SI) edifice began its construction through the Lower SI stage when massive lavas dated at ~45 ka formed a basal cone. During the Upper SI stage, the uppermost part of this edifice was destroyed by the highly explosive Jatuncama phase (VEI 5) leaving a 30-40 m-thick ignimbrite sequence. The subsequent extrusion of several dacitic lava domes reconstructed the South Iliniza summit at around 35 ka. The Terminal SI stage corresponds to the emission of several andesitic lavas between 31 ± 4 and 25 ± 3 ka. The Iliniza eruptive activity extended into the Late Pleistocene and Holocene with the extrusion of the Tishigcuchi lava dome, and the emission of the Pongo lava flow dated at 6 ± 4 ka. Based on the proposed eruptive history, we suggest that a revised volcanic hazard assessment of the potentially active Iliniza volcano is required.

1. INTRODUCTION

Magmatism in subduction zones archetypically creates volcanic arcs formed by large composite volcanoes whose erupted volumes reaches several tens of cubic kilometers (de Silva and Lindsay, 2015). After several geochronological studies, it seems that arc volcanoes grow in "spurts", i.e., relatively short-term construction stages separated by long-term quiescence periods. Inside these constructional periods, there are frequent "instantaneous" destruction events, such as sector collapses and caldera-forming eruptions (e.g., Esser et al., 2004; Hildreth, 2007; Conway et al., 2016; Pure et al., 2020). Indeed, several case studies worldwide attest the potential for eruptive activity to occur even after long-term quiescence periods (e.g., García-Palomo et al., 2002; Hora et al., 2007; Mariño et al., 2021). The study of the temporal, morphological and compositional records during the growth of a volcano provides insights into magmatic processes and eruptive behavior at various time scales, and thus represents a key issue for hazard assessment (Gamble et al., 2003; Capra et al., 2008; Brenna et al., 2012).

Although several suitable examples are found in the North and South American arcs, for instance, most studies are focused on recent time scales, leaving the oldest eruptive history poorly studied. Along the Ecuadorian Andes, at least 84 Quaternary volcanoes have been identified (Bernard and Andrade, 2011). These volcanic centers are arranged in north-south alignments, described from east to west as the Volcanic Front, the Main Arc, and the Back-Arc (Fig. 1; Hall and Beate, 1991; Hall et al., 2008). Each alignment shows distinctive characteristics in terms of magma composition, volcanic edifice morphology and eruptive dynamics. In particular, the Volcanic Front includes the edifices located on the Western Cordillera, with 15-20 km-wide composite volcanoes which showed several cone-building stages and major sector collapses (e.g., Pichincha volcanic complex; Robin et al., 2010). The formation of lava dome complexes is also recurrent, and often appears during the final eruptive stages following the transition from high-silica andesites to dacites (e.g., Hidalgo, 2006; Robin et al., 2010; Almeida et al., 2019; Bellver-Baca et al., 2020). Moreover, these stages also involve highly explosive eruptions (e.g., Hidalgo et al., 2008; Robin et al., 2008; Andrade et al., 2021), directed blast events (e.g., Bernard et al., 2014), and the formation of two 3 km-wide calderas (i.e., Cuicocha and

Quilotoa calderas; von Hillebrandt, 1989; Mothes and Hall, 2008; Sierra et al., 2020). Notably, large explosive eruptions occurred during the Holocene in the northern and central segments of the Volcanic Front (Fig. 1), where large urban areas such as Quito (Ecuador's capital city) are nowadays surrounded by a high number of volcanoes.

Iliniza is a twin-peaked compound volcano (5125 m asl) located 50 km south of Quito, in the central segment of the Ecuadorian Volcanic Front (Fig. 1a). Iliniza volcano exhibits volcanological characteristics that are similar to other Volcanic Front edifices, including the presence of dacite lava domes and a thick pyroclastic density current (PDC) deposit, both associated with its late eruptive stages (Hidalgo et al., 2007). Although the geochemistry of the Iliniza volcano's magmas was previously investigated (e.g., Hidalgo et al., 2007, 2012; Schiano et al., 2010; Georgatou et al., 2018), its eruptive chronology remained uncertain due to the lack of radioisotopic ages. Based on erosional geomorphology compared to other volcanoes in the Ecuadorian arc, Hidalgo et al. (2007) suggested that the earliest Iliniza activity might be as old as ~1 Ma, and Hall and Beate (1991) inferred an Holocene age for the Tishigcuchi satellite lava dome. Despite the lack of reliable chronological data, Iliniza volcano was classified as potentially active (Bernard and Andrade, 2011). If confirmed, a relatively young activity would increase the probability of a future reactivation and, consequently, increase the threat that this volcano may represent for the populations living in the Inter-Andean valley.

Here, we define the main geomorphologic and volcanological units of Iliniza volcano and present its first geochronological data, combined with new field observations and geomorphological reconstructions. We aim to constrain the eruptive stages of Iliniza volcano through time, as well as its growth and erosion patterns. In addition, geochemical data are used to describe the compositional evolution of its eruptive products over time. Our results show that the construction period of Iliniza volcano is shorter and younger than expected.

2. GEOLOGICAL CONTEXT

Iliniza volcano is part of the Northern Andean Volcanic Zone, which results from the subduction of the Nazca plate beneath the South American plate (Fig. 1a). The tectonic processes related to the active margin in Ecuador caused the formation of two N-S mountain ranges separated by a tectonic depression known as the Inter-Andean Valley (e.g., Tibaldi and Ferrari, 1992; Spikings et al., 2005; Winkler et al., 2005; Alvarado et al., 2016). Iliniza volcano (0°39.8'S, 78°43.0'W) is constructed on the boundary between the Western Cordillera and the Inter-Andean Valley. The Western Cordillera mainly consists of deformed oceanic mafic rocks accreted to the continental margin during the Late Cretaceous to Paleocene, which are covered by Paleogene sedimentary and volcano-sedimentary sequences (Jaillard et al., 2004; Vallejo et al., 2009, 2019). These units are in turn overlain by the Silante Formation, which is exposed to the northwest of Iliniza volcano. It is composed of volcanoclastic sandstones, conglomerates and red mudstones derived from the erosion of the San Juan de Lachas volcanic island arc, of Early Miocene age (Boland et al., 2000; Vallejo, 2007; Vallejo et al., 2020). Towards the southwest, the Zumbahua Formation constitutes an extensive volcanic and volcano-sedimentary sequence deposited in lacustrine and fluvial basins during the Late Miocene-Pliocene (Barberi et al., 1988; Hughes and Bermúdez, 1997; Vallejo et al., 2019). Although no radioisotopic ages are reported, a Pliocene age is inferred for the volcanoclastic series forming the plains gullied by the Jatuncama River, to the west of Iliniza (Hughes and Bermúdez, 1997).

The northern Andean geodynamics are dominated by the northeastward decoupling of the North Andean Sliver from the continental margin of South America (Freymueller et al., 1993; Witt et al., 2006; Egbue and Kellogg, 2010; Nocquet et al., 2014). Alvarado et al. (2016) observed that deformation in Ecuador has progressively migrated eastward to its current location on the Chingual-Cosanga-Pallatanga-Puna (CCPP) fault system creating the Quito-Latacunga Microblock (QL-M). Iliniza volcano is located along the NE-SW alignment created by the Machachi right-lateral strike-slip fault (M-f; Soulas et al., 1991; Egüez et al., 2003), and is close to the northern extension of the Latacunga reverse Fault System (Lavenu et al., 1995; Egüez et al., 2003). The M-fs is considered part of the Quito-Latacunga fault system which delineates the western boundary of the QL-M (Alvarado et al., 2016).

3. METHODS

3.1. Sampling strategy

Field work and sampling were carried out in 2019 and 2020 with the purpose to identify and describe the main volcanic units, to establish their stratigraphic relationships, and to collect new fresh rock samples for K-Ar dating and whole-rock geochemical analyses. In addition, in order to gather a comprehensive stratigraphic record, we used previous field data, petrographic descriptions, and samples from Hidalgo (2001, 2006) and Hidalgo et al. (2007).As a result, we completed a dataset of 113 whole-rock analyses that cover the entire stratigraphic succession Sample locations are shown in Figure 2. All maps and locations are projected using the Universal Transverse Mercator (UTM) coordinate system (Zone 17).

From the whole dataset, a total of nineteen new samples were selected for K-Ar dating from lava flows, monolithological breccias, and juvenile blocks from PDC deposits. Six samples belong to the North Iliniza edifice, of which two correspond to monolithological breccias located at the base of the northern flank (ILI 11, ILI 20), three to intermediate height lavas (ILI 16B, ILI 18, 19EQ17), and one to a summit lava (19EQ24). Four lavas of South Iliniza edifice were sampled from the northern (19EQ18, 19EQ25), eastern (19EQ02), southern (20EQ72) and southwestern (19EQ20, 20EQ75) flanks, as along with a lava dome sample (19EQ23b) and a massive lava block (ILI 29A, 20EQ79b) from the summit area. Three juvenile blocks were sampled from PDC's deposits on the northern flank of Iliniza (19EQ16), Jatuncama river valley (19EQ19a) and Santa Rosa area (20EQ81a). Lastly, four dacitic blocks were collected from the Pilongo (ILI 25) and Tishigcuchi (19EQ22, 19EQ70, 20EQ74) satellite lava domes. In addition, three samples of the nearby Santa Cruz volcano were taken from its southern (19EQ44) and northern (19EQ03, 20EQ69) flanks.

3.2. K-Ar dating

Eighteen samples were carefully selected based on their low weathering appraised from thin section examination (Appendix A). High groundmass abundance (relative to phenocrysts content), and low vesicle content were also considered. Samples were dated by applying the K-Ar method on groundmass, using the unspiked Cassignol-Gillot technique (Cassignol and Gillot, 1982). The latter relies on the detection of tiny quantities of radiogenic argon (^{40}Ar*) diluted by ^{40}Ar from atmospheric contamination. The mass spectrometer is used to measure the ^{40}Ar and ^{36}Ar electrical signals extracted from a sample, and to compare them with an aliquot of pure air measured under the same analytical conditions. This approach renders the knowledge of the atmospheric ^{40}Ar/^{36}Ar ratio unnecessary for our technique. The difference of the ^{40}Ar/^{36}Ar isotopic ratios acquired from the sample and the atmosphere is used to quantify the amount of ^{40}Ar* produced by the ^{40}K radioactive decay since the closure of the isotopic system. Thus, the independent measurement of K-content, the ^{40}K relative isotopic abundance in nature and its decay constant (Steiger and Jäger, 1977; Min et al., 2000) allow to calculate the age of the sample. The Cassignol-Gillot technique is adequate to date young calk-alkaline volcanic products that typically exhibit low ^{40}Ar* contents (Gillot et al., 2006). This technique was successfully applied to the Quaternary Ecuadorian volcanic arc (Alvarado et al., 2014; Bablon et al., 2018, 2019, 2020), in the Andes (e.g., Germa et al., 2010; Samaniego et al., 2016; Grosse et al., 2018, 2020; Pallares et al., 2019; Mariño et al., 2021), and worldwide (e.g., Germa et al., 2011; Hildenbrand et al., 2018; Dibacto et al., 2020). Groundmass fraction is preferred for dating since it is the potassium-enriched phase that crystallizes last following the eruption, and thus incorporated the initial argon with atmospheric isotopic ratio. Furthermore, the use of groundmass avoids the possible contamination by inherited ^{40}Ar* contained in phenocrysts, which could skew ages in young volcanic products (e.g., Singer et al., 1998; Harford et al., 2002; Renne et al., 2012; Lahitte et al., 2019). Samples were prepared following the protocols detailed in Bablon et al. (2018), where analytical procedures, standards used, and uncertainty calculations are also supplied. Potassium and argon isotopic measurements were carried out at the GEOPS laboratory in Orsay (Paris-Saclay University, France). The reproducibility under 1-σ confidence level was checked by performing the measurements at least twice. Fourteen new K-Ar ages were acquired from the previous selected samples and are presented in Table 1.

3.3. Geochemical analyses

Nineteen additional samples were collected for geochemical analyses, following the sampling strategy previously described, to provide a dataset of 40 new analyses presented in Appendix B. Whole-rock contents of major and trace elements were measured from agate-grinded powders at the GEO-OCEAN laboratory, University of Bretagne Occidental (Brest, France) via Inductively Coupled Plasma-Atomic Emission Spectrometry (ICP-AES), following the procedure described by Cotten et al. (1995). Relative standard deviations are <1% for SiO_2, <2 % for the other major elements, and < 5 % for trace elements. To provide a complete dataset covering as much of the volcanic history as possible, we included 73 analyses from Iliniza volcano obtained in the same laboratory and published by Hidalgo et al. (2007).

3.4. Geomorphological reconstructions

Numerical methods allow to model the primary geomorphology of a volcanic edifice despite the presence of intense erosive features. They are used to calculate the bulk volume of an edifice at the end of each construction stage, as well as the volume removed by erosion. The morpho-structural analyses were carried out using field observations, Google Earth® satellite images, orthophotography, and a 4-m spatial resolution digital elevation model (DEM) developed by the Sigtierras program from the Ministry of Agriculture and Livestock of Ecuador (http://geoportal.agricultura.gob.ec). A regular 30-m resolution point cloud was extracted from it to facilitate numerical calculations. We followed the method developed in Lahitte et al. (2012) according to the descriptions provided by Germa et al. (2015) and Dibacto et al. (2020), which are summarized below. The above-mentioned papers yield further methodological details and comparisons with other numerical techniques.

The surface preceding the Iliniza construction (S_{t0}) was calculated using an ordinary kriging interpolation method. Our approach uses the external points extracted from the basal outline of the edifice, and theorized profiles of the paleo-topography. The elevation uncertainty at each point is provided by the prediction standard error map resulting from ordinary kriging. We employed the ShapeVolc software (Lahitte et al., 2012) to model the post-cone-building surfaces S_{t1} based on control points extracted from reliable present-day remnants of pre-erosion topography such as the radial crests and *planèzes*. Uncertainty at each point is defined by $\sigma_{St1-i} = \sqrt{\sigma_{mod}^2 + \sigma_{ed-i}^2}$, where σ_{mod} is the elevation uncertainty of the modeled surface, and σ_{ed-i} is that derived from the spatial dispersion of the control points determined by a prediction standard error map.

The construction stage volume v_{cs} corresponds to the integration of the elevation difference between S_{t0} and S_{t1} surfaces multiplied by the pixel area, while the erosion stage volume v_{es} uses S_{t1} and present-day S_{t2} surfaces. Volume uncertainty σ_v is given by the combination of the height uncertainties of each point σ_{e-i} multiplied by the pixel area, where $\sigma_{e-i} = \sqrt{\sigma_{Stf-i}^2 + \sigma_{Sti-i}^2}$. Output ($R_o$) and erosion ($R_e$) rates are obtained by dividing the v_{cs} and v_{es} volumes by the eruptive ΔT_{cs} and quiescent ΔT_{es} period durations, respectively. Rate absolute uncertainty is defined by $\sigma_{Ri} = \sqrt{\left(\frac{\sigma_v}{v}\right)^2 + \left(\frac{\sigma_T}{\Delta T}\right)^2}$, where σ_T is the uncertainty of the period duration ΔT.

4. RESULTS

4.1. Morphology

The twin peaks of Iliniza volcano correspond to two prominent superimposed stratovolcanoes (Fig. 2). The **North Iliniza edifice** (5125 m asl), also called Tioniza (Hidalgo, 2001), stands on the eastern edge of the Western Cordillera at 4000 m asl. This volcano has an elongated basal shape with a radius ranging from 4 km over the Western Cordillera side to 6 km in the Inter-Andean Valley side. The summit's southeastern flank is not preserved. Only a narrow and steep amphitheater (750 m wide and slope angle > 40°), probably formed by glacial erosion, remains in place (Fig. 2b). The North Iliniza lavas partially cover the *Huayrapungo peak* (4585 m asl), a narrow pinnacle located 2.5 km northeast from the summit (Fig. 2b). The **South Iliniza edifice** (5248 m asl) covers the southeast flank of the North Iliniza edifice. This stratovolcano has a well-defined semicircular shape of 7 km of radius, whose summit is located 1.5 km to the southeast of North Iliniza's summit. The base of the volcano ranges from 3300 m asl to 3600 m asl in the inter-Andean valley. Lastly, the **Pilongo** and **Tishigcuchi** satellite lava domes are located at the northern and southern flanks of Iliniza volcano, about 5.2 km from its highest summit.

The late Pleistocene glaciations strongly modified the morphology of Iliniza volcano (Hidalgo, 2001), as shown by the different stages of glacial erosion exhibited by its two edifices. The northern edifice is dissected by wide U-shaped valleys creating a steep central horn surrounded by a low-sloping *plateau* situated between 4100 and 4200 m asl, where its lowest points extend down to 3780 m asl. Several well-defined ridges radiate from the central horn and separate each glacial valley (Fig. 3a). A succession of moraines a few tens of meters thick is observable inside the main glacial valleys at elevations ranging from 4100 m asl to 4500 m asl. The northwestern flank of the Huayrapungo peak is contoured by a succession of lateral moraines that form a glacial fan at the base of this structure, i.e., at about 4100 m asl at the head of the Pilongo Valley (Fig. 3b). In contrast, the South Iliniza glacial valleys are narrow and less incised preserving the conical shape of the edifice. The lowest frontal and lateral moraines are recognizable at the base of the cone at about 3700 m asl on the eastern flank and 3800 m asl on the northern and southern flanks. Heine (2011) presented a summary of evidences describing several glacial cycles in the Ecuadorian Andes (e.g., Clapperton, 1986, 1987; Heine, 1995, 2000). The author inferred that the non-studied moraine sequences of the Iliniza, Cayambe and Antisana volcanoes could include deposits from the Last Glacial Maximum (LGM; ~35-20 ka) and even from older cycles. This hypothesis is supported by the moraine associations identified at Rucu Pichincha volcano, where LGM and Younger Dryas (~12.5-10.2 ka) moraine series were recognized via radiocarbon dating in the interior of pre-existing wide glacial valleys between 4000 and 3800 m.asl. (Heine, 1995). Observed at similar elevations, the moraine sequences described at Chimborazo volcano and in the Papallacta valley (Chacana caldera; Fig. 1) have been attributed to the LGM and others possibly to previous glacial cycles (Clapperton, 1987, 1990; Heine, 1995). Comparing the moraine elevations in the Ecuadorian Andes, we also consider that those observed at Iliniza volcano were emplaced during the LGM (and possibly during earlier glacial cycles), where its northern edifice suffered a more extended erosion, thus explaining its more conspicuous erosional morphology. Nonetheless, further documentation is required to confirm the ages of these glacial deposits.

4.2. Eruptive Chronology

The evolution stages of Iliniza volcano and its relationship with the nearby Santa Cruz volcano are presented below, together with a simplified geological map shown in Figure 4. Volcanic units description is based on the previous studies of Hidalgo (2001, 2002) and Hidalgo et al. (2007), and our new morphologic, stratigraphic, and geochronological data summarized in Table 2.

4.2.1.Santa Cruz Volcano

Santa Cruz (SC), is a highly eroded stratovolcano (3978 m asl) mainly comprising successions of andesitic lava flows (e.g., 19EQ44: 56.4 wt.% SiO_2). It is located in the Inter-Andean valley, 10 km east of the South Iliniza edifice (Fig. 2). Only the southern flank of the volcano is exposed, where the preserved gently dipping slopes (8-14°) are dissected by wide and deep valleys. Highly weathered and altered dacitic lava domes are found in the summit area (e.g., 19EQ04: 65.6 wt.% SiO_2). The northern flank, where preserved, is covered by the Inter-Andean valley deposits (Qiv), which are 300 m higher compared to the *Qiv* average elevation at the base of the southern flank. A K-Ar age of 702 ± 11 ka is obtained from an andesitic lava flow of the southern ridge (19EQ44), representing an intermediate age of the Santa Cruz edifice.

Loma Saquigua **(LS)** is an isolated summit peak (3839 m asl) of Santa Cruz volcano. The base of Loma Saquigua is formed by a dacite lava dome (LS_D; 63.7 wt.% SiO_2). A block taken in its eastern flank (20EQ69) yields a relatively young K-Ar age of 79 ± 2 ka. The upper structure of Loma Saquigua consists of andesitic lava flows (LS_A; 57.8 wt.% SiO_2) dated at 60 ± 3 ka (19EQ03). The Santa Cruz volcanic products, including those of Loma Saquigua, show a mineral assemblage composed of plagioclase, orthopyroxene, clinopyroxene, and Fe-Ti oxides, whereas amphibole is more common in the dacitic lavas.

4.2.2.Iliniza Volcano

4.2.2.1. Early satellite lavas

The Pilongo lava dome (Pi) is located on the lower north-western flank of Iliniza volcano, along the western edge of the homonymous valley (Fig. 2). This satellite lava dome is 600 m in basal diameter and reaches a height of 3935 m asl., i.e., 250 m above the valley floor. Due to its low elevation and location, the lava dome does not show evidence of substantial glacial erosion. Erosion caused by fluvial processes created steep slopes on its eastern and southern flank. The northern and western flanks are surrounded by a gently sloping plain consistent in elevation and dip with the northern flank of Iliniza. The Pilongo lava dome is formed by porphyritic rhyodacites (68-69 wt. % SiO_2; Table 2). A sample taken from the southern base of the lava dome (ILI25) yields an age of 353 ± 6 ka.

4.2.2.2. North Iliniza edifice (NI)

This edifice is formed by two thick sequences of andesitic to dacitic (62-65 wt.% SiO_2) lava flows, monolithological breccias and scarce proximal pyroclastic deposits (Fig. 4; Table 2). The highest portion of the edifice is characterized by widespread hydrothermal alteration. In addition, the lavas sourced from the Huayrapungo satellite peak appear interspersed between the two above-mentioned sequences of North Iliniza.

The Lower NI stage (NI-Ls) is defined by a sequence of monolithological breccias,5-30 m-thick lava flows, and scare pyroclastic successions, displaying andesite to dacite compositions (62-64 wt.% SiO_2). This sequence is well exposed in the glacial ridges around the North Iliniza edifice specially on the Western Cordillera side (e.g., Quillotoro and Ninarrumi hills; Fig. 3a). The NI-Ls maximum thickness is estimated at 200-300 m in the Western Cordillera side, and 700-800 m in the Inter-Andean Valley side. The NI-Ls succession overlies the Mio-Pliocene volcano-sedimentary sequences of the Western Cordillera (i.e., Silante and Zumbahua Formations). Two blocks taken from two monolithological breccia layers (ILI20, ILI11) in the northern flank give ages of 122 ± 6 and 123 ± 6 ka.

The Huayrapungo stage (NI-Hs) is represented by an eroded peak formed by voluminous andesitic lavas (62 wt.% SiO_2) cropping out in the northern NI flank. Huayrapungo lavas exhibit meter-scaled flow banding textures, well-exposed in the southern flank of the peak (Fig. 4b), whereas flow foliation and subvertical columnar jointing are common close to the summit areas. Although field relationships are unclear, it seems that Huayrapungo lavas, of at least 250 m in thickness, overly a pyroclastic succession probably related to the Lower NI stage clearly observed in the southern flank of the Huayrapungo peak. Based on the morphological and structural characteristics of Huayrapungo and its stratigraphic position, we consider this peak as a satellite vent of the NI edifice. A sample (19EQ17) collected south of the Huayrapungo peak is dated at 121 ± 2 ka.

The Upper NI stage (NI-Us) consist of a 600–700 m-thick pile of viscous lava flows (30-60 m in thickness) that shape the upper structure of the North Iliniza edifice above 4400 m asl (Fig. 4a). This lava succession is andesite to dacite in composition (62-65 wt.% SiO_2). A notable feature is a voluminous 100 m-thick lava exposed in the summit area which flowed down 1500 m northwestwards (Fig. 3a). Erosion reveals the flow foliation structure and fractures associated with a secondary summit vent located at 4800 m asl. A sample collected at the base of this massive lava yields an age of 116 ± 2 ka (ILI18). Another 90 m-thick lava is located on the western flank in the Quillotoro hill, overlying the NI-Ls succession. It is cut by a glacial valley on its highest portion. We suggest an emplacement age similar to that of the ILI18 lava flow.

4.2.2.3. South Iliniza edifice (SI)

This edifice corresponds to a compound volcano formed by a basal stratovolcano discordantly overlain by a summit lava dome complex and massive lava flows (Fig. 5). These successions define the three cone-building stages of the South Iliniza edifice (Table 2). The lower flanks of the edifice are covered by a thick pyroclastic succession associated with the second stage.

The Lower SI stage (SI-Ls) corresponds to an early cone constructed on top of the NI successions and the remnants of the Santa Cruz volcano. It consists of a 1100 m-thick succession of dacitic (62-65 wt. % SiO_2) massive lavas, sparse inter-layered breccias, and semi-consolidated PDC deposits. Outcrops near the center of the edifice show moderated hydrothermal alteration. Two consistent ages of 45 ± 2 ka and 46 ± 1 ka are obtained from lavas located on the northern (19EQ18) and eastern (19EQ02) flanks, respectively. Glacial striations preserved on the northern lava flow confirm its pre-LGM age (roughly 35-20 ka; Clapperton, 1986; Heine, 2011). This basal stratovolcano is disrupted above 4700 m asl where the radial slope decreases top-down from 35° to less than 10° forming a truncated cone. The change in slope is especially noticeable on the southern flank where a saddle shape structure, called the Cantarilla height (Fig. 3a), marks a structural unconformity (Fig. 4a and 5b).

The Upper SI stage (SI-Us) incorporates a pyroclastic succession surrounding the lower flanks of the basal cone, and the summit lava domes located above the Cantarilla unconformity (Table 2).

The Jatuncama ignimbrite (SI-Ji) is a widespread PDC succession that crops out at the lower flanks of the South Iliniza edifice (Fig. 6). Widespread outcrops occur in the Jatuncama valley, to the southwest of Iliniza volcano (Fig: 4). The Jatuncama pyroclastic deposits overlie semi-consolidated pyroclastic deposits ascribed to the Lower SI stage to the east, and inorganic consolidated soils to the south of the SI edifice. The Jatuncama ignimbrite consists of a thick multiple bedded *block-and-ash PDC sequence* (SI-J_{BA}) overlaid by *pumice-and-ash flow deposits* (SI-J_{PA}). The SI-J_{BA} deposits are continuous, typically normal graded to massive, poorly sorted, slightly consolidated, and gray to pinkish in color. No interlayered paleosoils are observed in the Jatuncama sequence. Degassing pipes are commonly observed in the upper beds (Fig. 6b). The SI-J_{BA} deposits are constituted by poorly vesiculated juvenile dacite blocks (63-67 wt.% SiO_2; Table 2) showing radial and prismatical-jointed structures, and varying amounts of pumice lapilli. Both clast types are supported in a fine-grained ash-matrix bearing glass shards and free crystals of plagioclase, amphibole, and scarce pyroxene. Low-density pumice lapilli are generally scarce in the lower beds of the SI-J_{BA} deposit, whereas clasts with textural banding of glassy and high-density pumice are common (Fig. 6c). The SI-J_{BA} average thickness is ~30-40 m with a maximum of 120 m in the Jatuncama valley. The reconstructed area covered by the SI-J_{BA} deposits reaches ~60 km^2 with an average thickness of 35 m, yielding an estimated volume of

2.1 km^3. These values suggest an eruptive phase with a volcanic explosivity index (VEI) of at least 5. We should stress that no tephra fallout deposits have been observed, thus the estimated volume should be considered as a minimum. The high-density pumice sample (19EQ19a) collected from an intermediate bed of the SI-J$_{BA}$ in the Jatuncama valley exhibit high atmospheric contamination preventing K-Ar dating.

Two 7-10 m-thick pumice-and-ash PDC units (SI-J$_{PA}$) overlie the SI-J$_{BA}$ deposits at the Jatuncama valley (site 20EQ92; Fig. 6d) and the northeastern SI flank (site 20EQ96). The SI-J$_{PA}$ units are massive, poorly consolidated, and light gray to beige in color. They are composed of fibrous dacite pumice lapilli (65-67 wt.% SiO_2) and occasional high-density dacite blocks up to 10 cm in diameter (Fig. 6e), supported in a matrix formed by fine glass shards and crystals of plagioclase, amphibole, and pyroxene. In addition, a 25 cm-thick rhyolite pumice-and-ash flow PDC deposit (71-72 wt.% SiO_2) crops out on the northeastern SI flank was described as the *Santa Rosa pumice-and-ash PDC (SI-*J_{SR}*)* by Hidalgo et al. (2007). We identified a ~1-2 m-thick matrix-supported deposit (site 20EQ81), with a poorly-sorted texture, outcropping on top of the northern SI-J$_{PA}$ (site 20EQ96). The collected samples reveal a mixture of rhyolitic pumiceous blocks (20EQ81a) and poorly vesiculated dacite blocks (20EQ81b, c) all ranging from 10-30 cm in diameter, suggesting a probable reworking of the primary deposit described by Hidalgo et al. (2007).

The Jatuncama ignimbrite sequence is preserved as a gently sloping surface (4-12°) intersected by shallow fluvial channels. The heads of these streams are commonly covered by moraines or intersected by glacial valleys at elevations above ~3750 m asl, i.e., above the LGM limit observed in other volcanoes of the region (Clapperton, 1986, 1990; Heine, 2000, 2011). The Jatuncama succession is overlain by a thick sequence of paleosoils, tephra fallout deposits from Cotopaxi, and other reworked materials of broadly Holocene age (Fig. 5a). Notably, the Cotopaxi F2 and F4 rhyolitic tephra fall deposits (7770 ± 70 to 5830 ± 80 ^{14}C yr BP; Hall and Mothes, 2008) were identified in the Planchaloma and Pastocalle areas (Fig. 4). Minor landslide scarps affecting these shallow deposits are recognizable on the eastern and southeastern SI flanks.

Two *consolidated PDC deposits (SI-U_{CP})* crop out east of the Cantarilla height, on the southwestern flank of the cone (Fig. 4b). These deposits, which are ~100 m-thick each, overlie the Lower SI sequence forming the conspicuous Cantarilla angular unconformity. The summit lava domes and its related deposits overlie this pyroclastic sequence. Unfortunately, no samples could be collected due to the terrain roughness.

The Summit Lava Dome Complex (SI-U_{SDC}) is located on top of the remnants of the Lower SI edifice (Fig. 5b), between 4710 and 5060 m asl, reaching a basal diameter of ~1.7 km. The SI-U_{SDC} vent, inferred as the geometrical center of the structure, occurs 250 m to the north with respect to that of the basal cone. As a result of the erosion, only the main core of the summit lava domes has been preserved. Multiple lava lobes and remnants of the SI-U_{SDC} talus are exposed in the summit southern flank, forming a sequence of thinner strata lying unconformably upon the older cone in the Cantarilla height (Fig 5b). The summit lava domes are dacitic in composition (64–67 wt.% SiO_2) and. A sample taken at the northern base of the SI-U_{SDC} (19EQ23b) yields an age of 34 ± 1 ka. The higher sections of the South Iliniza edifice are covered by *undifferentiated dacitic breccias (SI-U_{DL})* interpreted as reworked PDC deposits related to the SI-U_{SDC} dome-forming eruptive activity.

The Terminal SI stage (SI-Ts) is represented by several massive lava flows and monolithological breccias that overlie the SI-U_{SDC} deposits and descend mainly along the western flank into the Providencia valley (Fig. 4b and 5). This lava succession shapes the SI edifice summit above 5000 m asl, reaching a thickness of ~250 m. The SI-Ts lavas are mostly andesitic in composition (SI-T_A; 61–63 wt.% SiO_2). Two voluminous lava flows, called the Termancucho lavas (Hidalgo, 2001), outcrop on the summit's western flank and can be traced 3 km downslope into the upper Providencia valley (Fig. 3a and 4b). The lower 70 m-thick lava flow (20EQ79) is composed by a porphyritic dacite (SI-T_D; ~67 wt.% SiO_2), whereas the upper 50 m-thick lava flow (ILI 29) has an andesitic composition (~62 wt.% SiO_2) consistent with the overlying SI-T_A series (Table 2). A sample collected from the lower Termancucho lava (20EQ79a) was discarded for K-Ar measurements due to its high phenocryst and low groundmass contents. Another andesitic lava flow outcrops on the southern SI flank at the headwaters of the Tiliche river (site 20EQ72; Fig. 4), is partially overlaid by a LGM moraine. The upstream trace of the Tiliche lava flow is intersected by the Providencia valley, hiding the source of this flow. Nevertheless, we relate this lava flow to the summit's terminal lavas given their similar petrological characteristics and stratigraphic position (Table 2). A sample taken from the base of the Tiliche lava flow (20EQ72) yields an age of 31 ± 4 ka. A comparable, albeit younger, age of 25 ± 3 ka was obtained from an andesitic block (19EQ25) collected from a monolithological breccia on the northern SI flank.

4.2.2.4. Late satellite lavas

Tishigcuchi (T), also called Rasuyacu (Hall and Beate, 1991), is a satellite dome *coulée* located on the southern flank of the South Iliniza edifice (Fig. 7a). It is composed of a 1100 m-wide lava dome (4185 m asl), and at least 3 viscous lava flows reaching 90 m-thick and 1800 m-long. The lava SI-J_{BA} was constructed over a 7° slope at 3850 m asl formed by the SI-J_{BA} and the Tiliche lava flow (Fig. 4). The Tishigcuchi lava *coulée* is andesitic in composition (62-63 wt.% SiO_2). No collapse or explosion crater structures are observed, and no pyroclastic deposits related to the Tishigcuchi lava dome are found in our study. The dome shows no evidence of glacial erosion and is covered by soils intercalated with Cotopaxi's rhyolitic Holocene lapilli and ash fall deposits. Attempts to obtain a K-Ar age from the selected samples (19EQ22, 20EQ74) were unsuccessful due to the high atmospheric contamination exhibited by the groundmass.

Pongo (Pg) is a voluminous lava forming a 4 km-long terrace between the Pongo and Providencia rivers, in the Jatuncama valley (Fig. 7b). The erosion caused by the Pongo river has exposed a 60-m-high cliff with columnar jointing at the southwestern edge of the lava. Exposures of the Jatuncama ignimbrite are observed on the valley walls next to the Pongo lava . The Pongo lava is composed by aphanitic andesites (59 wt.% SiO_2). Although the sample collected at the Providencia River (19EQ20) is highly contaminated by atmosphere, a second sample taken at the base of the columnar jointing exposures (20EQ75) provides an age of 6 ± 4 ka. The source of the lava flow cannot be clearly identified upstream into the glacially carved Providencia valley. Given the size of the Pongo lava and its Holocene age, its upper parts should be still observable as they could not have been completely eroded or covered by younger deposits. Thus, an origin from a satellite vent located at the southwestern base of Iliniza volcano is suspected.

4.3. Reconstructed morphology for volume estimations

4.3.1. Basement surface reconstruction

Defining the substratum morphology is an essential step for volume calculations, as minor changes in the basement morphology could lead to volume errors greater than 50% in stratovolcanoes (e.g., Ceboruco volcano; Frey et al., 2004; Tungurahua volcano; Bablon et al., 2018). The basement shape of Iliniza volcano (S_{I-t0} surface) was reconstructed using a theorized topographic profile modeled from four parallel auxiliary profiles located to the north and to the south of the volcano . The auxiliary profiles intersect the hills of Ninarrumi and Quillotoro to the north, and Chilcapamba to the south of the Iliniza volcano (Fig. 2 and 8a), which form the northwestern-southeastern ridge of the Western Cordillera. Further to the east, at the eastern and southeastern foothills of the South Iliniza edifice, the auxiliary profiles intersect a slight elevation of the Santa Cruz volcano and the Loma La Cruz ridge (Fig. 8a).

4.3.2. Iliniza volcano paleosurface reconstruction and volume calculations

The total reconstructed area for Iliniza volcano is 127 km^2, which corresponds to a present-day bulk volume of 34 ± 14 km^3. This volume represents the amount of volcanic products preserved between the present-day topography and the modeled basement surface S_{I-t0}. Considering an activity range of 98 ± 7 kyr, corresponding to the growth of the North and South Iliniza edifices between 123 ± 6 ka and 25 ± 3 ka, an apparent bulk output rate of 0.35 ± 0.14 km^3/kyr was determined. Nevertheless, our results have shown that the eruptive activity of Iliniza volcano was seemingly interrupted by long-term quiescence periods between each construction stage. Therefore, volume calculations, and growth or output rates, require to be adjusted for each construction and erosion stages (Table 2). Appendix C provides several topographic profiles comparing the modeled cones of the Iliniza edifices, the modeled basement surface, and the present-day surface.

The first construction stage of the Iliniza volcano corresponds to the extrusion of the Pilongo lava dome, which has a present-day volume of 18 ± 5 × 10^{-3} km^3. The next stage corresponds to the construction of the North Iliniza edifice. The modeled cone S_{NI-t1} has a semicircular base with a concave profile that reached 5200 m asl. The symmetry axis is located 200 m southwest of the present-day summit and is coincident with the narrow amphitheater of the eastern flank. The volume of the modeled cone v_{NI-cs} is 28 ± 9 km^3, a relatively small value compared to the volcano's heigh of ~1700 m above the Inter-Andean Valley. This value is explained by the presence of the Western Cordillera basement, which makes its base level ~400 m higher than the Inter-Andean valley. Considering a period of activity occurring between 124 ± 5 ka and 116 ± 2 ka, the output rate obtained R_{NI-o} is 3.5 ± 2.6 km^3/kyr.

La Virgen plain (LV), located northeast of Iliniza volcano (Fig. 2 and 5), was originally interpreted as part of the South Iliniza edifice (Hidalgo et al., 2007). However, a detailed analysis of its geometry reveals that the slope gradient direction of La Virgen points to a source located to the west, coinciding with the location of the North Iliniza edifice. We support this hypothesis by the discordant position of the northern lava flow from the SI-Ls stage (19EQ18, ILI 34). This lava flowed into the Pilongo valley between La Virgen plain and the Huayrapungo peak (Fig. 4), implying a pre-South Iliniza construction for the northeastern sector. Overlapping of other products of the South Iliniza edifice is not excluded during the formation of La Virgen plain.

The reconstruction of the eastern sector of the North Iliniza edifice at ~45 ka (i.e., before South Iliniza construction) was not straightforward given that this area is covered by the South Iliniza deposits. This area completes the surface S_{NI-t2} corresponding to the relief at the end of the quiescence period between growth of both edifices. We used two auxiliary topographic profiles based on radial sections of the present-day northeastern sector La Virgen and the southwestern sector Pongo alto (Fig. 8b) to compute the surface S_{NI-t2}. The eroded volume v_{NI-es}, calculated between the modeled cone S_{NI-t1}

and the eroded surface S_{NI-t2}, is 6 ± 2 km^3. Only the western sector was exposed to non-stop weathering during the ~116 kyr quiescence of North Iliniza. Then, the eroded volume in the western sector v_{es-W} is 3 ± 1 km^3, implying an erosion rate R_{NI-e-W} of 0.03 ± 0.01 km^3/kyr.

The construction of the South Iliniza edifice comprises the lower cone-building, the upper cone-building, and the terminal effusive stages. The former two cones were modeled independently as a first approach, but we selected a simpler geometry involving a single cone given the poor geometric constrains. A volume v_{SI-cs} of 18 ± 6 km^3 was obtained for the modeled cone S_{SI-t1}. As in the case of the North edifice, this volume appears to be rather small given the volcano height of ~1850 m measured from the Inter-Andean valley bottom. The modeled paleo-summit is located 250 m east of the current summit and reaches 5300 m asl. Considering a 21 ± 3 kyr-long cone-building period (from 46 ± 1 to 25 ± 3 ka), the South Iliniza edifice yields an output rate R_{SI-o} of 0.8 ± 0.3 km^3/kyr. The volume difference between the present-day surface S_{SI-t2} and the reconstructed cone S_{SI-t1} gives an eroded volume v_{SI-es} of 6 ± 2 km^3 implying an erosion rate R_{SI-e} of 0.24 ± 0.09 km^3/kyr. Figure 8c shows that the northern contact between the South Iliniza modeled cone and the partially eroded North Iliniza edifice occurs along the Rio Blanco valley in the northern sector and along the Pongo Alto valley in the southern sector (see also Fig. 11c-f). Lastly, the Tishigcuchi lava dome yields a present-day volume of 339 ± 41 × 10^{-3} km^3, whereas the Pongo lava flow reaches a volume of 73 ± 18 × 10^{-3} km^3.

4.4. Geochemical characterization

The Iliniza volcanic products are classified in the SiO_2 vs. K_2O diagram (Fig. 9a; Peccerillo and Taylor, 1976) as medium-K andesites and dacites, which are similar to those observed in other Volcanic Front edifices (VF, Fig. 1b). Some scarce andesites and rhyolites, corresponding to the Pongo and Santa Rosa units, fall outside the VF field. Each construction stage shows narrow silica content ranges. Negative correlations are observed in Harker diagrams including MgO, Fe_2O_3*, CaO, TiO_2 and Al_2O_3 *versus* silica, used as differentiation index, while K_2O and Na_2O show positive correlations (Fig. D.1). The North Iliniza and South Iliniza eruptive products typically form well-defined trends. Samples from the Pilongo and Santa Rosa units plots along or near the prolongation of the Iliniza trend. In contrast, the eruptive products of Tishigcuchi and Pongo show K_2O enrichment and Na_2O depletion compared to the andesitic lavas of the Terminal SI stage(SI-T_A).

Variations in trace element contents in relation to silica increase for the North and South Iliniza tend to form well-correlated trends (Fig. D.2). Some transition metals (e.g., V, Sc) show a marked compatible behavior as well as Heavy Rare-Earth Elements (HREE; e.g., Yb) and Y. However, the Large-Ion Lithophile Elements contents (LILE; e.g., Rb, Ba) remain relatively constant, except for South Iliniza edifice which shows an overall incompatible behavior with the andesitic SI-Ts values being the lowest. High contents of Light Rare-Earth Elements (LREE; e.g., La, Ce), Th and Sr are observed in the products of Santa Rosa, Tishigcuchi and Pongo. Cr and Ni are also high for these samples, as well as in the andesitic SI-Ts lavas. Only a few samples are available for lower South Iliniza edifice, making its geochemical signature poorly constrained. Its northern lava flow (19EQ18, ILI 34) exhibits unusually high LREE, Th and Sr contents.

Incompatible elements and Rare-Earth Elements (REE) spider diagrams normalized to primitive mantle/chondrites (Sun and McDonough, 1989) are shown in Figure 9b-e. Overall, the chondrite-normalized REE diagram for North and South Iliniza dacites exhibit similar, slightly fractionated patterns with LREE enrichment and HREE depletion, and no Eu anomaly. The South Iliniza samples present an overall, albeit slight, REE depletion relative to North Iliniza, except for the northern Lower SI stage lava flow (19EQ18, ILI 34) which has a strong LREE enrichment. The highest HREE depletions are observed for the most evolved products of Iliniza volcano, i.e., the dacitic Termancucho lava (dacitic SI-Ts), Pilongo and Santa Rosa units. The primitive mantle-normalized plot reveals a similar pattern for all samples with positive Ba, K and Rb anomalies and negative Nb and P. Lower Ti, Dy, Y and Yb signatures characterize the dacitic SI-Ts, Pilongo and Santa Rosa units. The low HREE (e.g., $Yb<0.61$ ppm) and Y (<7.8 ppm) concentrations observed in the Pilongo and Santa Rosa units, coupled with the high LREE (e.g., $La>12$ ppm) contents, result in elevated La/Yb ratios compared to other units (Fig 10e). Conversely, samples from the Tishigcuchi and Pongo eruptive products show similar ratios but also higher mafic signatures (e.g., $SiO_2<63$ wt.%, Mg#>50). Overall, the La/Yb ratio show a slight increase over time (excluding Pilongo), whereas fluid-mobile to fluid-immobile ratios (e.g., Ba/Th) decrease (Fig. 10b, d). Further detailed descriptions regarding the geochemistry and petrography of Iliniza volcano are provided in Hidalgo (2001, 2002) and Hidalgo et al. (2007).

5. DISCUSSION

5.1. Iliniza and Santa Cruz geochronological evolution

Although a rather limited number of ages have been obtained here, their key stratigraphic position allows us to propose a complete geochronological evolution of Iliniza and Santa Cruz volcanoes. Our stratigraphic, geochronological, and geochemical data suggest that the Iliniza volcano had a relatively short lifetime span. We propose that Iliniza volcano was constructed in short eruptive intervals separated by long repose periods throughout late Pleistocene (from ~350 ka to the Holocene) as summarized below. Prior to the construction of the Iliniza volcano, the Santa Cruz volcano was constructed in the Inter-Andean valley. The predominantly effusive activity of the Santa Cruz volcano, dated at 702 ± 11 ka, is represented by the thick lavas exposed on its southern flank and the dacitic lava domes present in the summit area. We found no other evidence of volcanic activity in this area until the extrusion of the Pilongo lava dome, the earliest stage of Iliniza volcano, which took place close to the Machachi fault (Fig. 3) at 353 ± 6 ka.

After an apparent quiescence period of ~230 kyr, the North Iliniza volcano started the construction of a ~1600 m-high edifice, in the southern prolongation of the Machachi fault (Fig. 11a). Two lava successions characterize the effusive activity occurring between 123 ± 6 and 116 ± 2 ka (Table 1), after the Penultimate Glacial Maximum (Shackleton et al., 2003). Nevertheless, we interpret this age range with caution as no basal lava could be sampled. Based on morphological and stratigraphic evidence, we attribute the formation of the Huayrapungo peak to a satellite vent contemporary with the lower lava sequence. Later, the erosion caused by Pleistocene glaciations, presumably from pre-LGM glacial cycles (>49 ka; Heine, 2011), shaped the wide radial glacial valleys around the North Iliniza summit, and incised the Pilongo and Providencia-Pongo paleo-valleys (Fig. 4). After an apparent ~620 kyr-long quiescence period, activity resumed on the Santa Cruz volcano when the dacitic lava dome of Loma Saquigua was extruded at 79 ± 2 ka, followed by the emission of andesitic lavas at 60 ± 3 ka (Fig. 11b).

The South Iliniza edifice was constructed on top of the partially eroded North Iliniza. A conspicuous structural unconformity marks the two growth phases of this edifice. The earliest phase corresponds to the emplacement of the Lower SI stage eruptive products, which are constituted by thick lavas and pyroclastic successions dated at about 45 ka, forming a basal edifice (Fig. 11c). Remnants of this edifice are exposed in the southern flank and in the center of the South Iliniza edifice. According to the stratigraphic position of the Jatuncama ignimbrite deposits covered by LGM moraines, and its radial distribution fanning away from the South Iliniza edifice, we propose that this unit represents an explosive phase prior to the second growth phase of this edifice (Fig. 11d). As discussed below, the geochemistry of the dacitic components of the Jatuncama ignimbrite is comparable to the SI summit lava domes (SI-U_{SDC} unit), thus supporting our hypothesis. During the second growth phase, a summit lava dome complex and its related pyroclastic deposits subsequently filled the depression caused by the Jatuncama eruption (crater rim, Fig. 4) and reconstructed the volcanic cone since 34 ± 1 ka. Then, a final mostly effusive stage involved the emission of several andesitic lavas covering the uppermost parts of the volcanic cone (Fig. 11e). Our K-Ar ages suggest that this activity extended up to 25 ± 3 ka.

The Tishigcuchi lava dome coulée and Pongo lava flow extrusions represent the youngest eruptive stages of the Iliniza volcano (Fig. 11f), as previously suggested (Hall and Beate, 1991). The Tishigcuchi lava dome was extruded on the southern flank of the volcano along the southern prolongation of the Machachi fault. Although no radiometric age could be obtained, a stratigraphic age between 20 to 8 ka can be proposed due to the presence of the underlying Tiliche lava flow dated at 31 ± 4 ka, the lack of LGM glacial erosion or associated deposits (maximum extents reached at 34.8-27.9 ka and 19.2 ka; Heine, 2011), and the overlying Cotopaxi F2 and F4 fallout deposits (~8.5 and ~6.7 cal ka; Hall and Mothes, 2008). Finally, the age obtained from the Pongo lava flow (6 ± 4 ka) demonstrates that Iliniza volcano was still active during the Holocene.

The available ages in the central part of the Ecuadorian arc point to the existence of two types of volcanism based on the extent of their eruptive chronology. The long-lived volcanic complexes, which exhibit multiple edifices and cone-building stages as old as 1 Ma, extending their activity to more recent times even up to the Holocene (e.g., Pichincha and Cayambe volcanic complexes; Samaniego et al., 2005; Robin et al., 2010), and the short-lived compound volcanoes, which were rather formed in briefer cone-building stages of few tens of ka and were mostly emplaced in relatively recent times (e.g., Cotacachi and Imbabura volcanoes; Le Pennec et al., 2011; Almeida et al., 2019). Our new K-Ar ages reveal that the age and extent of Iliniza volcanic activity is in good agreement with this group of young short-lived volcanoes, whereas Santa Cruz could be considered as a long-lived volcano.

5.2. The Jatuncama explosive phase

The Jatuncama ignimbrite samples exhibit a dacitic composition similar to that of the South Iliniza upper stage (Fig. 12). However, the compositional dispersion of the SI-J_{BA} points to a more intricate deposit, as indicated by the SiO_2 content ranging between 63 and 67 wt.%. Figures 12a and 12b show the geochemical distribution of the SI-J_{BA} dacitic juvenile clasts compared to the South Iliniza units. For similar SiO_2 and Mg# values, the low-density pumices are slightly enriched in K_2O compared to the high-density pumices and dacites. Furthermore, the high-density pumices generally fall within the SI-U_{SDC} field, while low-density pumices are more correlated with the SI-T_D pole. The few glassy juvenile clasts available are relatively scattered without any clear relationship. The SI-J_{BA} composition also shows slight variations according to the location of the sampling site (Fig. 12d). A relatively higher dispersion degree is observed in the Jatuncama valley and on the southern flank (sites 7-9) compared to the southeastern flank where low K_2O samples seem to be absent (sites 3-5). This difference may be explained by the fact that the lower SI-J_{BA} beds, with higher participation of high-density pumices and dacites, are not well exposed on the southeastern flank. In addition, the plots of the SI-J_{PA} units (20EQ92, 20EQ96) fall in the fields of slightly K_2O enriched clasts. Therefore, on the basis of this geochemical evidence, the petrographic descriptions provided above, and the fact that neither discordances, nor interlayered paleosoils are observed in the Jactuncama succession, we argue that the

Jatuncama ignimbrite units correspond to an intricate deposit formed during an explosive dome-forming eruption followed by a pumiceous phase both associated with the upper SI stage, as suggested by Hidalgo et al. (2007). The Jatuncama eruption was followed by the extrusion of the Summit Lava Dome Complex (SI-U_{SDC}). Based on the estimated volume of the Jatuncama deposits, we infer the formation of a 1.5-2 km-wide crater (Figures 4 and 11d) related to the Jatuncama explosive phase (minimum VEI ~5), which agrees with the top surface diameter of the truncated basal cone (i.e., SI-Ls). The Cantarilla discordance marks the inferred crater rim created during the Jatuncama explosive phase (Fig. 11d).

In the lack of direct measurement, geomorphological, stratigraphic, and geochemical data can provide an approximate age for the Jatuncama ignimbrite. Considering that the SI-Ji sequence overlies the SI-Ls deposits and its distribution around the basal SI edifice, a lower bound is defined by the Lower SI stage at 45 ± 2 ka. The overlaying Tiliche lava flow (20EQ72) constrains the upper bound at 31 ± 1 ka. Such pre-LGM age is supported by the glacial morphology affecting the highest sections of the ignimbrite deposit, and by the thick Holocene tephra fallout sequence. Finally, considering the geochemical affinity with the SI-U_{SDC} unit, we propose that the Jatuncama explosive phase, and the formation of the SI-Ji pyroclastic sequence, occurred shortly before the extrusion of the summit lava domes dated at 34 ± 1 ka (19EQ23b).

5.3. Growth and erosion patterns of Iliniza Volcano

Volcanic edifices are composed of a wide variety of eruptive products including lava flows, lava domes, PDC successions, and fallout deposits accumulated around a central vent. The destruction of part of the volcanic edifice during highly explosive events and/or sector collapses, and the re-mobilization of unconsolidated materials are other factors to consider during or in between the growth phases. Therefore, the bulk volume of the main edifice does not represent the entire volcanic products emitted and thus the calculated values should be considered as minima. Nevertheless, volumes obtained in numerical reconstructions provide a first-order approximation, allowing recognition of fluctuations in its spatial and temporal output patterns, and allowing comparison with other eruptive centers, as discussed below.

According to our numerical reconstructions both Iliniza edifices reached similar heights and volumes. The combined v_{cs} volumes of the Iliniza edifices and satellite lava domes reaches a total bulk volume of 46 ± 15 km^3 of accumulated material (Table 2). This value includes the volume of material removed by erosion during the quiescence periods (v_{es}). About 61 vol.% of this volume belongs to the North Iliniza edifice, 38 vol.%. to the South Iliniza edifice, and the remaining 1 vol.% to the satellite lavas. Due to the complex topography of the Iliniza basement, our results exhibit a relatively high uncertainty of ~35 vol.%. The volume of the SI-Ji deposits is implicitly included in our calculations as its estimated value is within the volume uncertainty range.

The bulk volume of Iliniza volcano is similar to those reported for the other compound volcanoes located at the Ecuadorian northern cross-arc segment, e.g., Cushnirumi, Cusin, Fuya-Fuya and Imbabura, which range from 31 ± 19 km^3 to 61 ± 24 km^3 (Bablon et al., 2020). Large volcanic complex such as Pichincha, Cayambe and Mojanda accumulated larger volumes ranging from 115 ± 5 to ~160 km^3 (Robin et al., 2010; Samaniego et al., 2005; Bablon et al., 2020), which is not the case of Iliniza volcano. In contrast, Antisana has a bulk volume of ~61 km^3, but has a lifespan longer than 400 ka (Hall et al., 2017b). Volcanoes with volumes similar to those of Iliniza volcano are also found in the southern cross-arc segment. Effectively, each Iliniza edifice is comparable in volume to the Mulmul or Huisla stratovolcanoes, which show values of 22 ± 7 and 25 ± 11 km^3 (Bablon et al., 2018, 2020). Nevertheless, Iliniza volcano has a smaller volume relative to Chimborazo (Samaniego et al., 2012) and the whole Tungurahua (Bablon et al., 2018) volcanoes. Compared to other worldwide volcanoes, Iliniza could be considered as a medium-size compound volcano, whose volume and shape are typical of continental arcs (Grosse et al., 2009). Similar bulk volumes to Iliniza are found in volcanoes such as Parinacota (Hora et al., 2007), Ampato-Sabancaya (Samaniego et al., 2016), Yucamane-Calientes (Rivera et al., 2020), Ceboruco (Frey et al., 2004), or Katmai (Hildreth et al., 2003b) volcanoes. Nonetheless, the lifespans of these volcanoes differ by several tens of thousands of years.

The output rates calculated for the North Iliniza (3.5 ± 2.6 km^3/kyr) and South Iliniza (0.8 ± 0.3 km^3/kyr) edifices are quite variable, although both structures show comparable volumes and shapes. The higher growth rate of North Iliniza is explained by the short range of activity displayed by our radiometric ages. The lack of outcrops and/or sampling of the lower units might have biased the activity range towards the late-stage ages, then, the impact on output rates can be significant. Nevertheless, the sampling distribution and the small age range observed do not exclude a short-term (few tens of ka) construction of the North Iliniza edifice. In fact, high growth rates have also been documented for several Ecuadorian volcanoes such as Cubilche, Cusin, Imbabura (Bablon et al., 2020), Tungurahua III (Bablon et al., 2018), Cotopaxi (Hall and Mothes, 2008), and Guagua Pichincha (Robin et al., 2010) volcanoes, with R_o values ranging from 2.0 ± 1.5 to 3.6 ± 2.1 km^3/kyr. In contrast, the South Iliniza growth rate is comparable to those of other Ecuadorian arc volcanoes. R_o values between 0.6 ± 0.3 and 0.8 ± 0.2 km^3/kyr were reported for volcanoes such as Pichincha (Robin et al., 2010), Tungurahua I and II (Bablon et al., 2018), Mulmul (Bablon et al., 2019), and Chimborazo (Samaniego et al., 2012). Similar output rates were reported for other Andean volcanoes such as Misti (Thouret et al., 2001), Parinacota (Hora et al., 2007), and Ampato-Sabancaya (Samaniego et al., 2016); although they are comparatively higher than in other continental arc systems such as the Cascades Range, Central Andes, Mexico, Japan, or Alaska (e.g., Crisp, 1984; Hildreth et al., 2003a, 2003b; Frey et al., 2004; Ownby et al., 2007). Output rate comparisons should be taken with caution as R_o values (> 1-2 km^3/kyr) are typical of short-term growth episodes (of few ka), whereas low values are typical of bulk eruptive rates (i.e., long periods including the quiescensde periods; Bablon et al., 2020).

The eruptive history of the Iliniza edifices developed separately in time, in contrast to other twin-peaked volcanoes such as Mojada-Fuya Fuya (Robin et al., 2009) in the Ecuadorian arc, or Yucamane-Calientes (Rivera et al., 2020) in the Peruvian arc. In fact, the evolution of Iliniza and Santa Cruz volcanoes included long-lasting quiescence periods, which is also the case for other volcanoes in the Ecuadorian Andes such as Cotopaxi (Hall and Mothes, 2008), Pichincha (Robin et al., 2010), Atacazo-Ninahuilca (Hidalgo, 2006), and Tungurahua (Bablon et al., 2018). Long resting periods (several tens of thousands of years) are also reported in other twin volcanoes and compound volcanoes in the region and worldwide such as San Pedro-San Pablo (Bertin and Amigo, 2015; González-Maurel et al., 2019), Ampato-Sabancaya (Samaniego et al., 2016), Yucamane-Calientes (Rivera et al., 2020), and Colima (Robin et al., 1987; Cortés et al., 2010). These observations suggest that eruptive hiatuses are also common in this type of compound volcanoes from volcanic arcs, contrasting with models of sustained eruptive activity throughout their lifetimes (e.g., Conway et al., 2016; Pure et al., 2020), while increasing the potential for reactivation in present-day dormant volcanoes.

5.4. Overall geochemical nature

Overall, samples from the North and South Iliniza (NS-I) edifices exhibit rather little geochemical variability along a single evolutive trends (Fig. A.1) suggesting neither a change in magmatic sources nor in the magmatic process active at crustal levels. In contrast, important differences rise when NS-I trace element contents are compared to the early and late satellite lavas and the Santa Rosa rhyolites, in which HREE depletions and LREE enrichments were identified. Notably, the Iliniza rocks do not show a continuous increase in SiO_2 or decrease in Mg# over time (Fig. 10a) as observed at other volcanoes from the central segment of the arc (e.g., Pichincha volcano; Robin et al., 2010). The silica-poor units (i.e., SI-T_A, T and Pg units) occur during the late evolutionary stages of Iliniza.

As presented in Table 2, the common mineral assemblages exhibit by the North Iliniza lavas include plagioclase, orthopyroxene, clinopyroxene, Fe-Ti oxides and scarce amphibole, whereas the South Iliniza eruptive products include plagioclase, amphibole, clinopyroxene, Fe-oxides and rare orthopyroxene. Based on a geochemical modelling approach, Hidalgo et al. (2007) and Schiano et al. (2010) proposed that the NS-I magmatic series could result from an amphibole-dominated fractional crystallization process of typical calc alkaline arc magmas. Their models also showed that the silica-rich products of Pilongo and Santa Rosa units require more complex petrogenetical models. In fact, the trace element contents of these units were unable to be reconciled with a parental melt with NS-I composition through a single fractional crystallization process, thus, implying the occurrence of an additional parental melt and a mixing process involving both magmas. The petrogenetic processes related to the origin of such silica-rich magmas are widely discussed as they could be produced by several processes including partial melting of the subducted slab and the metasomatism of the mantle wedge caused by the derived silicate melts (e.g., Bourdon et al., 2003; Samaniego et al., 2005, 2010; Hidalgo et al., 2007, 2012), crustal melting and/or assimilation of the lower crust (Garrison and Davidson, 2003; Garrison et al., 2006; Sainlot et al., 2020), and intra-crustal fractionation of the required high-pressure assemblages (e.g., Bryant et al., 2006; Chiaradia et al., 2009; Bellver-Baca et al., 2020). However, a comprehensive analysis of these petrogenetic processes and their temporal behavior is beyond the scope of this paper. Nonetheless, the whole Iliniza magmatic series could be thus explained by a fractional crystallization process coupled with magma mixing between mafic and silica-rich end-members (Hidalgo et al., 2007; Schiano et al., 2010); where the geochemical signatures of both end-members seem to occur throughout the geochronological evolution of Iliniza volcano, rather than being restricted to its final stages.

5.5. Exploring the implications for the hazard assessment

Unlike other active and potentially active volcanoes from the Volcanic Front (e.g., Pululahua, Guagua Pichincha, Ninahuilca), whose eruptions involved dacitic magmas and dome-forming eruptive dynamics, the Holocene activity of Iliniza mainly released andesitic lavas. Based on the proposed eruptive chronology, we infer that the most probable eruptive scenario could be dominated by the emission of lava flows and/or the formation of low-viscosity lava domes, whose subsequent collapse may produce PDCs and regional tephra fallout deposits. The apparent migration of the active vents through time, from northern to southern locations, favors an eruptive scenario possibly taking place on the southern flank of Iliniza volcano. However, an active vent located in higher areas close to the summit cannot be discarded. In such case, an eruption in these steeper slope areas would favor the destabilization of the newly emitted lavas increasing the risk of PDC formation, potentially accompanied by explosive phases and widespread tephra fallouts (Voight et al., 2002; Harnett et al., 2018). Such events could affect the 200,000 inhabitants living within 20 km of the volcano (INEC, 2010), including the populations of Chaupi, Pastocalle and Toacazo (Fig. 2).

Although a high explosive phase was identified at Iliniza volcano, this event was unique throughout its eruptive history and are absent in the Holocene eruptive chronology. Therefore, we expect that a scenario involving a highly explosive eruption (e.g., VEI 5), such as the Jatuncama event, is less probable in the short term. In addition, the Iliniza eruptive history does not include any major flank collapse, as no avalanche deposits or morphological remains suggesting a collapse amphitheater were identified. However, the occurrence of the Iliniza volcano above an active strike-slip fault system, the potential weakening of its flanks caused by weathering and hydrothermal alteration, and the steeply inclined slopes of its uppermost areas increase the risk of a potential collapse promoted by a tectonic event.

Finally, the Cotopaxi fallout deposits covering the Iliniza volcano slopes is an additional hazard to consider, although it is not intrinsically related to the Iliniza activity. The Holocene tephra layers deposited on the flanks of Iliniza could be easily remobilized, especially during the rainy season (December to April), forming secondary lahars that flow into the ravines of the volcano. The Cotopaxi tephra sequence, reaching up to 10 m in thickness, may slide due to the low cohesion of the lower and thicker tephra layers. This hazard is supported by the multiple landslide deposits observed on the southern flank of the Santa Cruz volcano (Hall et al., 2017a), and by the small scarps observed on the east and southeast slopes of the South Iliniza edifice.

6. CONCLUSIONS

This work provides the first geochronological data for the Iliniza volcano and allows to establish a comprehensive overview of its development over time. The first volcanic manifestations in the area correspond to the adjacent Santa Cruz volcano dated at 702 ± 11 ka. After a long quiescent period, its activity resumed at 79 ± 2 ka and 60 ± 3 ka forming the small-volume Loma Saquigua lava dome.

Iliniza shows a young episodic activity that began with the extrusion of the rhyodacite Pilongo lava dome occurring at 353 ± 6 ka. The Iliniza compound volcano (46 ± 15 km^3) comprises two andesitic to dacitic edifices formed in several cone-building stages. The older North Iliniza edifice (28 ± 19 km^3)

was first constructed by a succession of thin lavas and breccias during the Lower NI stage at 123-122 ka, followed by the formation of the Huayrapungo satellite peak at 121 ± 2 ka. Then, thick viscous lava sequence dated at 116 ± 2 ka built the higher portion of the edifice through the Upper NI stage. The North Iliniza edifice showed a relatively high output rate of 3.5 ± 2.6 km^3/kyr.

After a ~70 kyr quiescence period, the South Iliniza edifice (18 ± 6 km^3) grew over the remnants of the North Iliniza edifice in three main cone-building stages, with an output rate of 0.8 ± 0.3 km^3/kyr. A basal edifice was constructed during the Lower SI stage by a series of massive lavas of dacitic composition, dated between 46 ± 1 and 45 ± 2 ka. The Upper SI stage started with the Jatuncama explosive phase, in which the uppermost portion of the basal stratovolcano was destroyed and a 30-40 m-thick dacitic pyroclastic succession was deposited. The estimated minimum bulk volume of the Jatuncama ignimbrite deposits is 2.1 km^3, corresponding to a VEI ~5 eruption. The subsequent eruptive activity rebuilt the South Iliniza edifice with the emplacement of a summit lava dome complex and its related PDC deposits. The Terminal SI stage corresponds to the emission of several lava flows of andesitic composition dated between 31 ± 4 and 25 ± 3 ka. Finally, higher K andesite magmas were emitted from satellite vents located to the south of Iliniza forming the Tishigcuchi lava dome probably in the Holocene, and the Pongo lava flow dated at 6 ± 4 ka. Contrary to other volcanoes of the volcanic front, the Iliniza magmas show a compositional transition from dacites (63-67 wt.% SiO_2) to andesites (60-63 wt.% SiO_2) in the later eruptive stages. Based on these lines of geological and geochronological evidences, we support the hypothesis that the Iliniza volcano must be considered as a potentially active volcanic center.

Acknowledgments

The authors wish to thank Brad Singer and Georges Boudon, and an anonymous reviewer, for their detailed reviews, constructive comments, and suggestions, which helped us to improve this manuscript. The authors are grateful to the “Reserva Ecológica Ilinizas” members for sampling authorization and logistics. We also thank Patricio Ramon for useful discussions and for authorizing the use of his aerial photographic material, as well as Valérie Godard for having manufactured all the thin sections. This work is part of an Ecuadorian-French cooperation program carried out between the Instituto Geofísico, Escuela Politécnica Nacional (IGEPN), Quito, Ecuador, and the French Institut de Recherche pour le Développement (IRD), thought the Laboratoire Mixte International “Séismes et Volcans dans les Andes du Nord” (LMI-SVAN) program. This work was supported by the CNRS/INSU TelluS and the LMI-SVAN programs. The first author’s PhD grant was funded by the “Secretaria Nacional de Educación Superior, Ciencia, Tecnología e Innovación” (SENESCYT), Ecuador. This is Laboratoire de Géochronologie Multi-Techniques (LGMT) contribution number 169 and Laboratory of Excellence ClerVolc contribution number XXX.

REFERENCES

Almeida, M., Bablon, M., Andrade, D., Hidalgo, S., Quidelleur, X., Samaniego, P., 2019. New constraints on the geological and chronological evolution of the Cotacachi-Cuicocha Volcanic Complex (Ecuador). Presented at the 8th International Symposium on Andean Geodynamics (ISAG), Quito, Ecuador.

Alvarado, A., Audin, L., Nocquet, J.M., Jaillard, E., Mothes, P., Jarrín, P., Segovia, M., Rolandone, F., Cisneros, D., 2016. Partitioning of oblique convergence in the Northern Andes subduction zone: Migration history and the present-day boundary of the North Andean Sliver in Ecuador. Tectonics 35, 1048–1065. https://doi.org/10.1002/2016TC004117

Alvarado, A., Audin, L., Nocquet, J.M., Lagreulet, S., Segovia, M., Font, Y., Lamarque, G., Yepes, H., Mothes, P., Rolandone, F., Jarrín, P., Quidelleur, X., 2014. Active tectonics in Quito, Ecuador, assessed by geomorphological studies, GPS data, and crustal seismicity. Tectonics 33, 67–83. https://doi.org/10.1002/2012TC003224

Andrade, S.D., Müller, A.V., Vasconez, F.J., Beate, B., Aguilar, J., Santamaría, S., 2021. Pululahua dome complex, Ecuador: eruptive history, total magma output and potential hazards. Journal of South American Earth Sciences 106, 103046. https://doi.org/10.1016/j.jsames.2020.103046

Bablon, M., Quidelleur, X., Samaniego, P., Le Pennec, J.-L., Audin, L., Jomard, H., Baize, S., Liorzou, C., Hidalgo, S., Alvarado, A., 2019. Interactions between volcanism and geodynamics in the southern termination of the Ecuadorian arc. Tectonophysics 751, 54–72. https://doi.org/10.1016/j.tecto.2018.12.010

Bablon, M., Quidelleur, X., Samaniego, P., Le Pennec, J.-L., Lahitte, P., Liorzou, C., Bustillos, J.E., Hidalgo, S., 2018. Eruptive chronology of Tungurahua volcano (Ecuador) revisited based on new K-Ar ages and geomorphological reconstructions. Journal of Volcanology and Geothermal Research 357, 378–398. https://doi.org/10.1016/j.jvolgeores.2018.05.007

Bablon, M., Quidelleur, X., Samaniego, P., Le Pennec, J.-L., Santamaría, S., Liorzou, C., Hidalgo, S., Eschbach, B., 2020. Volcanic history reconstruction in northern Ecuador: insights for eruptive and erosion rates on the whole Ecuadorian arc. Bull Volcanol 82, 11. https://doi.org/10.1007/s00445-019-1346-1

Barberi, F., Coltelli, M., Ferrara, G., Innocenti, F., Navarro, J.M., Santacroce, R., 1988. Plio-quaternary volcanism in Ecuador. Geological Magazine 125, 1–14.

Bellver-Baca, M.T., Chiaradia, M., Beate, B., Beguelin, P., Deriaz, B., Mendez-Chazarra, N., Villagómez, D., 2020. Geochemical evolution of the Quaternary Chachimbiro Volcanic Complex (frontal volcanic arc of Ecuador). Lithos 356–357, 105237. https://doi.org/10.1016/j.lithos.2019.105237

Bernard, B., Andrade, D., 2011. Volcanes Cuaternarios del Ecuador Continental. IGEPN Poster Informativo.

Bernard, B., Hidalgo, S., Robin, C., Beate, B., Quijozaca, J., 2014. The 3640–3510 BC rhyodacite eruption of Chachimbiro compound volcano, Ecuador: a violent directed blast produced by a satellite dome. Bull Volcanol 76, 1–20. https://doi.org/10.1007/s00445-014-0849-z

Bertin, D., Amigo, Á., 2015. Geología y peligros del volcán San Pedro, II Región. Presented at the XIV Congreso Geologico Chileno, La Serena, Chile, pp. 128–131.

Boland, M., Ibadango, E., Pilatasig, L.F., McCourt, W., Aspden, J.A., Hughen, R., Beate, B., 2000. Geology of the Cordillera Occidental of Ecuador between 0°00’ and 1°00’N (No. 10), Proyecto de Desarrollo Minero y Control Ambiental. Cogidem - Brithis Geological Survey, Quito.

Bourdon, E., Eissen, J.-P., Gutscher, M.-A., Monzier, M., Hall, M.L., Cotten, J., 2003. Magmatic response to early aseismic ridge subduction: the Ecuadorian margin case (South America). Earth and Planetary Science Letters 205, 123–138. https://doi.org/10.1016/S0012-821X(02)01024-5

Brenna, M., Cronin, S.J., Smith, I.E.M., Sohn, Y.K., Maas, R., 2012. Spatio-temporal evolution of a dispersed magmatic system and its implications for volcano growth, Jeju Island Volcanic Field, Korea. Lithos 148, 337–352. https://doi.org/10.1016/j.lithos.2012.06.021

Bryant, J.A., Yogodzinski, G.M., Hall, M.L., Lewicki, J.L., Bailey, D.G., 2006. Geochemical Constraints on the Origin of Volcanic Rocks from the Andean Northern Volcanic Zone, Ecuador. Journal of Petrology 47, 1147–1175. https://doi.org/10.1093/petrology/egl006

Capra, L., Norini, G., Groppelli, G., Macías, J.L., Arce, J.L., 2008. Volcanic hazard zonation of the Nevado de Toluca volcano, México. Journal of Volcanology and Geothermal Research 176, 469–484. https://doi.org/10.1016/j.jvolgeores.2008.04.016

Cassignol, C., Gillot, P.-Y., 1982. Range and effectiveness of unspiked potassium-argon dating: experimental groundwork and applications, in: Odin, G.S. (Ed.), Numerical Dating in Stratigraphy. John Wiley & Sons, pp. 159–179.

Chiaradia, M., Müntener, O., Beate, B., Fontignie, D., 2009. Adakite-like volcanism of Ecuador: lower crust magmatic evolution and recycling. Contrib Mineral Petrol 158, 563–588. https://doi.org/10.1007/s00410-009-0397-2

Clapperton, C.M., 1990. Glacial and volcanic geomorphology of the Chimborazo-Carihuairazo Massif, Ecuadorian Andes. Earth and Environmental Science Transactions of The Royal Society of Edinburgh 81, 91–116. https://doi.org/10.1017/S0263593300005174

Clapperton, C.M., 1987. Maximal extent of late Wisconsin glaciation in the Ecuadorian Andes. Quaternary of South America and Antarctic Peninsula 5, 165–179.

Clapperton, C.M., 1986. Glacial geomorphology, Quaternary glacial sequence and palaeoclimatic inferences in the Ecuadorian Andes, in: Gardiner, V. (Ed.), International Geomorphology, Part II. Wiley, London, pp. 843–870.

Conway, C.E., Leonard, G.S., Townsend, D.B., Calvert, A.T., Wilson, C.J.N., Gamble, J.A., Eaves, S.R., 2016. A high-resolution 40Ar/39Ar lava chronology and edifice construction history for Ruapehu volcano, New Zealand. Journal of Volcanology and Geothermal Research 327, 152–179. https://doi.org/10.1016/j.jvolgeores.2016.07.006

Cortés, A., Garduño Monroy, V., Macías, J., Navarro-Ochoa, C., Komorowski, J.-C., Saucedo, R., Gavilanes Ruiz, J., 2010. Geologic mapping of the Colima volcanic complex (Mexico) and implications for hazard assessment. Special Paper of the Geological Society of America 464, 249–264. https://doi.org/10.1130/2010.2464(12)

Cotten, J., Le Dez, A., Bau, M., Caroff, M., Maury, R.C., Dulski, P., Fourcade, S., Bohn, M., Brousse, R., 1995. Origin of anomalous rare-earth element and yttrium enrichments in subaerially exposed basalts: Evidence from French Polynesia. Chemical Geology 119, 115–138. https://doi.org/10.1016/0009-2541(94)00102-E

Crisp, J.A., 1984. Rates of magma emplacement and volcanic output. Journal of Volcanology and Geothermal Research 20, 177–211. https://doi.org/10.1016/0377-0273(84)90039-8

de Silva, S., Lindsay, J.M., 2015. Chapter 15 - Primary Volcanic Landforms, in: Sigurdsson, H. (Ed.), The Encyclopedia of Volcanoes (Second Edition). Academic Press, Amsterdam, pp. 273–297. https://doi.org/10.1016/B978-0-12-385938-9.00015-8

DeMets, C., Gordon, R.G., Argus, D.F., 2010. Geologically current plate motions. Geophysical Journal International 181, 1–80. https://doi.org/10.1111/j.1365-246X.2009.04491.x

Dibacto, S., Lahitte, P., Karátson, D., Hencz, M., Szakács, A., Biró, T., Kovács, I., Veres, D., 2020. Growth and erosion rates of the East Carpathians volcanoes constrained by numerical models: Tectonic and climatic implications. Geomorphology 368, 107352. https://doi.org/10.1016/j.geomorph.2020.107352

Egbue, O., Kellogg, J., 2010. Pleistocene to Present North Andean “escape.” Tectonophysics 489, 248–257. https://doi.org/10.1016/j.tecto.2010.04.021

Egüez, A., Alvarado, A., Yepes, H., Machette, M.N., Costa, C., Dart, R.L., 2003. Database and map of Quaternary faults and folds of Ecuador and its offshore regions. US Geological Survey Open-File Report 03-289 71. https://doi.org/10.3133/ofr03289

Esser, R.P., Kyle, P.R., McIntosh, W.C., 2004. 40Ar/39Ar dating of the eruptive history of Mount Erebus, Antarctica: volcano evolution. Bull Volcanol 66, 671–686. https://doi.org/10.1007/s00445-004-0354-x

Frey, H.M., Lange, R.A., Hall, C.M., Delgado-Granados, H., 2004. Magma eruption rates constrained by 40Ar/39Ar chronology and GIS for the Ceboruco–San Pedro volcanic field, western Mexico. GSA Bulletin 116, 259–276. https://doi.org/10.1130/B25321.1

Freymueller, J.T., Kellogg, J.N., Vega, V., 1993. Plate Motions in the north Andean region. Journal of Geophysical Research: Solid Earth 98, 21853–21863. https://doi.org/10.1029/93JB00520

Gamble, J.A., Price, R.C., Smith, I.E.M., McIntosh, W.C., Dunbar, N.W., 2003. 40Ar/39Ar geochronology of magmatic activity, magma flux and hazards at Ruapehu volcano, Taupo Volcanic Zone, New Zealand. Journal of Volcanology and Geothermal Research 120, 271–287. https://doi.org/10.1016/S0377-0273(02)00407-9

García-Palomo, A., Macías, J.L., Arce, J.L., Capra, L., Garduño, V.H., Espíndola, J.M., 2002. Geology of Nevado de Toluca Volcano and surrounding areas, central Mexico. Geological Society of America Map and Chart Series, MCH089 26.

Garrison, J., Davidson, J., Reid, M., Turner, S., 2006. Source versus differentiation controls on U-series disequilibria: Insights from Cotopaxi Volcano, Ecuador. Earth and Planetary Science Letters 244, 548–565. https://doi.org/10.1016/j.epsl.2006.02.013

Garrison, J.M., Davidson, J.P., 2003. Dubious case for slab melting in the Northern volcanic zone of the Andes. Geology 31, 565–568. https://doi.org/10.1130/0091-7613(2003)031<0565:DCFSMI>2.0.CO;2

Georgatou, A., Chiaradia, M., Rezeau, H., Wälle, M., 2018. Magmatic sulphides in Quaternary Ecuadorian arc magmas. Lithos 296–299, 580–599. https://doi.org/10.1016/j.lithos.2017.11.019

Germa, A., Lahitte, P., Quidelleur, X., 2015. Construction and destruction of Mont Pelée volcano: Volumes and rates constrained from a geomorphological model of evolution. Journal of Geophysical Research: Earth Surface 120, 1206–1226. https://doi.org/10.1002/2014JF003355

Germa, A., Quidelleur, X., Gillot, P.Y., Tchilinguirian, P., 2010. Volcanic evolution of the back-arc Pleistocene Payun Matru volcanic field (Argentina). Journal of South American Earth Sciences 29, 717–730. https://doi.org/10.1016/j.jsames.2010.01.002

Germa, A., Quidelleur, X., Lahitte, P., Labanieh, S., Chauvel, C., 2011. The K–Ar Cassignol–Gillot technique applied to western Martinique lavas: A record of Lesser Antilles arc activity from 2Ma to Mount Pelée volcanism. Quaternary Geochronology 6, 341–355. https://doi.org/10.1016/j.quageo.2011.02.001

Gillot, P.Y., Hildenbrand, A., Lefèvre, J.C., Albore-Livadie, C., 2006. The K/Ar dating method: principle, analytical techniques, and application to Holocene volcanic eruptions in Southern Italy. Acta Vulcanologica 18, 55–66.

González-Maurel, O., Godoy, B., le Roux, P., Rodríguez, I., Marín, C., Menzies, A., Bertin, D., Morata, D., Vargas, M., 2019. Magmatic differentiation at La Poruña scoria cone, Central Andes, northern Chile: Evidence for assimilation during turbulent ascent processes, and genetic links with mafic eruptions at adjacent San Pedro volcano. Lithos 338–339, 128–140. https://doi.org/10.1016/j.lithos.2019.03.033

Grosse, P., Ochi Ramacciotti, M.L., Escalante Fochi, F., Guzmán, S., Orihashi, Y., Sumino, H., 2020. Geomorphology, morphometry, spatial distribution and ages of mafic monogenetic volcanoes of the Peinado and Incahuasi fields, southernmost Central Volcanic Zone of the Andes. Journal of Volcanology and Geothermal Research 401, 106966. https://doi.org/10.1016/j.jvolgeores.2020.106966

Grosse, P., Orihashi, Y., Guzmán, S.R., Sumino, H., Nagao, K., 2018. Eruptive history of Incahuasi, Falso Azufre and El Cóndor Quaternary composite volcanoes, southern Central Andes. Bull Volcanol 80, 1–26. https://doi.org/10.1007/s00445-018-1221-5

Grosse, P., Vries, B. van W. de, Petrinovic, I.A., Euillades, P.A., Alvarado, G.E., 2009. Morphometry and evolution of arc volcanoes. Geology 37, 651–654. https://doi.org/10.1130/G25734A.1

Gutscher, M.-A., Malavieille, J., Lallemand, S., Collot, J.-Y., 1999. Tectonic segmentation of the North Andean margin: impact of the Carnegie Ridge collision. Earth and Planetary Science Letters 168, 255–270. https://doi.org/10.1016/S0012-821X(99)00060-6

Hall, M.L., Beate, B., 1991. El volcanismo plio cuaternario en los Andes del Ecuador, in: El paisaje volcánico de la sierra ecuatoriana: geomorfología, fenómenos volcánicos y recursos asociados, Estudios de Geografia. Corporación Editora Nacional, Quito, pp. 5–17.

Hall, M.L., Mothes, P., 2008. The rhyolitic–andesitic eruptive history of Cotopaxi volcano, Ecuador. Bull Volcanol 70, 675–702. https://doi.org/10.1007/s00445-007-0161-2

Hall, M.L., Mothes, P., Vallance, J., Alvarado, A., 2017a. Deslizamientos del Yacupungo, in: Cabero, A., Zúñiga, M.A., Le Pennec, J.-L., Narváez, D., Hernández, M.J., Nocquet, J.M., Gómez, F.V. (Eds.), Memorias VIII Jornadas En Ciencias de La Tierra. Presented at the VIII Jornadas en Ciencas de la Tierra, EPN Editorial, Quito, Ecuador, pp. 85–87.

Hall, M.L., Mothes, P.A., Samaniego, P., Militzer, A., Beate, B., Ramón, P., Robin, C., 2017b. Antisana volcano: A representative andesitic volcano of the eastern cordillera of Ecuador: Petrography, chemistry, tephra and glacial stratigraphy. Journal of South American Earth Sciences 73, 50–64. https://doi.org/10.1016/j.jsames.2016.11.005

Hall, M.L., Samaniego, P., Le Pennec, J.L., Johnson, J.B., 2008. Ecuadorian Andes volcanism: A review of Late Pliocene to present activity. Journal of Volcanology and Geothermal Research, Recent and active volcanism in the Ecuadorian Andes 176, 1–6. https://doi.org/10.1016/j.jvolgeores.2008.06.012

Harford, C.L., Pringle, M.S., Sparks, R.S.J., Young, S.R., 2002. The volcanic evolution of Montserrat using 40Ar/39Ar geochronology. Geological Society, London, Memoirs 21, 93–113. https://doi.org/10.1144/GSL.MEM.2002.021.01.05

Harnett, C.E., Thomas, M.E., Purvance, M.D., Neuberg, J., 2018. Using a discrete element approach to model lava dome emplacement and collapse. Journal of Volcanology and Geothermal Research 359, 68–77. https://doi.org/10.1016/j.jvolgeores.2018.06.017

Heine, K., 2011. Chapter 57 - Late Quaternary Glaciations of Ecuador, in: Ehlers, J., Gibbard, P.L., Hughes, P.D. (Eds.), Developments in Quaternary Sciences, Quaternary Glaciations - Extent and Chronology. Elsevier, pp. 803–813. https://doi.org/10.1016/B978-0-444-53447-7.00057-X

Heine, K., 2000. Tropical South America during the Last Glacial Maximum: evidence from glacial, periglacial and fluvial records. Quaternary International, Quaternary palaeohydorlogy of South America 72, 7–21. https://doi.org/10.1016/S1040-6182(00)00017-3

Heine, K., 1995. Late Quaternary glacier advances in the Ecuadorian Andes: a preliminary report. Quaternary of South America and Antarctic Peninsula 9, 1–22.

Hidalgo, S., 2006. Les intéractions entre magmas calco-alcalins “classiques” et adakitiques: exemple du complexe volcanique Atacazo-Ninahuilca (Equateur) (Ph.D. thesis). Université Blaise Pascal - Clermont-Ferrand II, Clermont-Ferrand, France.

Hidalgo, S., 2002. Géochimie du complexe volcanique des Iliniza: pétrogenèse de séries à affinité adakitique de l’arc équatorien (DEA Report). Université Blaise Pascal, Clermont-Ferrand.

Hidalgo, S., 2001. Estudio geovolcanológico del complejo volcánico Iliniza (Engineer memoir). Escuela Politécnica Nacional, Quito.

Hidalgo, S., Gerbe, M.C., Martin, H., Samaniego, P., Bourdon, E., 2012. Role of crustal and slab components in the Northern Volcanic Zone of the Andes (Ecuador) constrained by Sr–Nd–O isotopes. Lithos 132–133, 180–192. https://doi.org/10.1016/j.lithos.2011.11.019

Hidalgo, S., Monzier, M., Almeida, E., Chazot, G., Eissen, J.-P., van der Plicht, J., Hall, M.L., 2008. Late Pleistocene and Holocene activity of the Atacazo–Ninahuilca Volcanic Complex (Ecuador). Journal of Volcanology and Geothermal Research 176, 16–26. https://doi.org/10.1016/j.jvolgeores.2008.05.017

Hidalgo, S., Monzier, M., Martin, H., Chazot, G., Eissen, J.-P., Cotten, J., 2007. Adakitic magmas in the Ecuadorian Volcanic Front: Petrogenesis of the Iliniza Volcanic Complex (Ecuador). Journal of Volcanology and Geothermal Research 159, 366–392. https://doi.org/10.1016/j.jvolgeores.2006.07.007

Hildenbrand, A., Marques, F.O., Catalão, J., 2018. Large-scale mass wasting on small volcanic islands revealed by the study of Flores Island (Azores). Scientific Reports 8, 13898. https://doi.org/10.1038/s41598-018-32253-0

Hildreth, W., 2007. Quaternary Magmatism in the Cascades: Geologic Perspectives. U.S. Geological Survey.

Hildreth, W., Fierstein, J., Lanphere, M., 2003a. Eruptive history and geochronology of the Mount Baker volcanic field, Washington. GSA Bulletin 115, 729–764. https://doi.org/10.1130/0016-7606(2003)115<0729:EHAGOT>2.0.CO;2

Hildreth, W., Lanphere, M.A., Fierstein, J., 2003b. Geochronology and eruptive history of the Katmai volcanic cluster, Alaska Peninsula. Earth and Planetary Science Letters 214, 93–114. https://doi.org/10.1016/S0012-821X(03)00321-2

Hora, J.M., Singer, B.S., Wörner, G., 2007. Volcano evolution and eruptive flux on the thick crust of the Andean Central Volcanic Zone: 40Ar/39Ar constraints from Volcán Parinacota, Chile. GSA Bulletin 119, 343–362. https://doi.org/10.1130/B25954.1

Hughes, R.A., Bermúdez, R., 1997. Geology of the Cordillera Occidental of Ecuador between 0°00’ and 1°00’S (No. 4), Proyecto de Desarrollo Minero y Control Ambiental. Cogidem - Brithis Geological Survey, Quito.

INEC, 2010. Censo de Población y Vivienda 2010 [WWW Document]. Instituto Nacional de Estadística y Censos, Ecuador. URL https://www.ecuadorencifras.gob.ec/base-de-datos-censo-de-poblacion-y-vivienda-2010/ (accessed 5.20.20).

Jaillard, E., Ordoñez, M., Suárez, J., Toro, J., Iza, D., Lugo, W., 2004. Stratigraphy of the late Cretaceous–Paleogene deposits of the cordillera occidental of central ecuador: geodynamic implications. Journal of South American Earth Sciences 17, 49–58. https://doi.org/10.1016/j.jsames.2004.05.003

Lahitte, P., Dibacto, S., Karátson, D., Gertisser, R., Veres, D., 2019. Eruptive history of the Late Quaternary Ciomadul (Csomád) volcano, East Carpathians, part I: timing of lava dome activity. Bull Volcanol 81, 27. https://doi.org/10.1007/s00445-019-1286-9

Lahitte, P., Samper, A., Quidelleur, X., 2012. DEM-based reconstruction of southern Basse-Terre volcanoes (Guadeloupe archipelago, FWI): Contribution to the Lesser Antilles Arc construction rates and magma production. Geomorphology, Volcano Geomorphology: landforms, processes and hazards 136, 148–164. https://doi.org/10.1016/j.geomorph.2011.04.008

Lavenu, A., Winter, T., Dávila, F., 1995. A Pliocene–Quaternary compressional basin in the Interandean Depression, Central Ecuador. Geophysical Journal International 121, 279–300. https://doi.org/10.1111/j.1365-246X.1995.tb03527.x

Le Pennec, J.L., Ruiz, A.G., Eissen, J.P., Hall, M.L., Fornari, M., 2011. Identifying potentially active volcanoes in the Andes: Radiometric evidence for late Pleistocene-early Holocene eruptions at Volcán Imbabura, Ecuador. Journal of Volcanology and Geothermal Research 206, 121–135. https://doi.org/10.1016/j.jvolgeores.2011.06.002

Mariño, J., Samaniego, P., Manrique, N., Valderrama, P., Roche, O., van Wyk de Vries, B., Guillou, H., Zerathe, S., Arias, C., Liorzou, C., 2021. The Tutupaca volcanic complex (Southern Peru): Eruptive chronology and successive destabilization of a dacitic dome complex. Journal of South American Earth Sciences 109, 103227. https://doi.org/10.1016/j.jsames.2021.103227

Min, K., Mundil, R., Renne, P.R., Ludwig, K.R., 2000. A test for systematic errors in 40Ar/39Ar geochronology through comparison with U/Pb analysis of a 1.1-Ga rhyolite. Geochimica et Cosmochimica Acta 64, 73–98. https://doi.org/10.1016/S0016-7037(99)00204-5

Mothes, P.A., Hall, M.L., 2008. The plinian fallout associated with Quilotoa's 800 yr BP eruption, Ecuadorian Andes. Journal of Volcanology and Geothermal Research, Recent and active volcanism in the Ecuadorian Andes 176, 56–69. https://doi.org/10.1016/j.jvolgeores.2008.05.018

Nocquet, J.-M., Villegas-Lanza, J.C., Chlieh, M., Mothes, P.A., Rolandone, F., Jarrin, P., Cisneros, D., Alvarado, A., Audin, L., Bondoux, F., Martin, X., Font, Y., Régnier, M., Vallée, M., Tran, T., Beauval, C., Mendoza, J.M.M., Martinez, W., Tavera, H., Yepes, H., 2014. Motion of continental slivers and creeping subduction in the northern Andes. Nature Geoscience 7, 287–291. https://doi.org/10.1038/ngeo2099

Ownby, S., Delgado Granados, H., Lange, R.A., Hall, C.M., 2007. Volcán Tancítaro, Michoacán, Mexico, 40Ar/39Ar constraints on its history of sector collapse. Journal of Volcanology and Geothermal Research 161, 1–14. https://doi.org/10.1016/j.jvolgeores.2006.10.009

Pallares, C., Quidelleur, X., Debreil, J.A., Antoine, C., Sarda, P., Tchilinguirian, P., Delpech, G., Gillot, P.-Y., 2019. Quaternary evolution of the El Tromen volcanic system, Argentina, based on new K-Ar and geochemical data: Insights for temporal evolution of magmatic processes between arc and back-arc settings. Journal of South American Earth Sciences 90, 338–354. https://doi.org/10.1016/j.jsames.2018.12.022

Peccerillo, A., Taylor, S.R., 1976. Geochemistry of eocene calc-alkaline volcanic rocks from the Kastamonu area, Northern Turkey. Contr. Mineral. and Petrol. 58, 63–81. https://doi.org/10.1007/BF00384745

Pure, L.R., Leonard, G.S., Townsend, D.B., Wilson, C.J.N., Calvert, A.T., Cole, R.P., Conway, C.E., Gamble, J.A., Smith, T. 'Bubs,' 2020. A high resolution 40Ar/39Ar lava chronology and edifice construction history for Tongariro volcano, New Zealand. Journal of Volcanology and Geothermal Research 403, 106993. https://doi.org/10.1016/j.jvolgeores.2020.106993

Renne, P.R., Mulcahy, S.R., Cassata, W.S., Morgan, L.E., Kelley, S.P., Hlusko, L.J., Njau, J.K., 2012. Retention of inherited Ar by alkali feldspar xenocrysts in a magma: Kinetic constraints from Ba zoning profiles. Geochimica et Cosmochimica Acta 93, 129–142. https://doi.org/10.1016/j.gca.2012.06.029

Rivera, M., Samaniego, P., Vela, J., Le Pennec, J.-L., Guillou, H., Paquette, J.-L., Liorzou, C., 2020. The eruptive chronology of the Yucamane-Calientes compound volcano: A potentially active edifice of the Central Andes (southern Peru). Journal of Volcanology and Geothermal Research 393, 106787. https://doi.org/10.1016/j.jvolgeores.2020.106787

Robin, C., Eissen, J.-P., Samaniego, P., Martin, H., Hall, M., Cotten, J., 2009. Evolution of the late Pleistocene Mojanda–Fuya Fuya volcanic complex (Ecuador), by progressive adakitic involvement in mantle magma sources. Bulletin of Volcanology 71, 233–258. https://doi.org/10.1007/s00445-008-0219-9

Robin, C., Mossand, P., Camus, G., Cantagrel, J.-M., Gourgaud, A., Vincent, P.M., 1987. Eruptive history of the Colima volcanic complex (Mexico). Journal of Volcanology and Geothermal Research 31, 99–113. https://doi.org/10.1016/0377-0273(87)90008-4

Robin, C., Samaniego, P., Le Pennec, J.-L., Fornari, M., Mothes, P., van der Plicht, J., 2010. New radiometric and petrological constraints on the evolution of the Pichincha volcanic complex (Ecuador). Bull Volcanol 72, 1109–1129. https://doi.org/10.1007/s00445-010-0389-0

Robin, C., Samaniego, P., Le Pennec, J.-L., Mothes, P., van der Plicht, J., 2008. Late Holocene phases of dome growth and Plinian activity at Guagua Pichincha volcano (Ecuador). Journal of Volcanology and Geothermal Research, Recent and active volcanism in the Ecuadorian Andes 176, 7–15. https://doi.org/10.1016/j.jvolgeores.2007.10.008

Sainlot, N., Vlastélic, I., Nauret, F., Moune, S., Aguilera, F., 2020. Sr–Pb isotopes signature of Lascar volcano (Chile): Insight into contamination of arc magmas ascending through a thick continental crust. Journal of South American Earth Sciences 101, 102599. https://doi.org/10.1016/j.jsames.2020.102599

Samaniego, P., Barba, D., Robin, C., Fornari, M., Bernard, B., 2012. Eruptive history of Chimborazo volcano (Ecuador): A large, ice-capped and hazardous compound volcano in the Northern Andes. Journal of Volcanology and Geothermal Research 221–222, 33–51. https://doi.org/10.1016/j.jvolgeores.2012.01.014

Samaniego, P., Martin, H., Monzier, M., Robin, C., Fornari, M., Eissen, J.-P., Cotten, J., 2005. Temporal Evolution of Magmatism in the Northern Volcanic Zone of the Andes: The Geology and Petrology of Cayambe Volcanic Complex (Ecuador). Journal of Petrology 46, 2225–2252. https://doi.org/10.1093/petrology/egi053

Samaniego, P., Rivera, M., Mariño, J., Guillou, H., Liorzou, C., Zerathe, S., Delgado, R., Valderrama, P., Scao, V., 2016. The eruptive chronology of the Ampato–Sabancaya volcanic complex (Southern Peru). Journal of Volcanology and Geothermal Research 323, 110–128. https://doi.org/10.1016/j.jvolgeores.2016.04.038

Samaniego, P., Robin, C., Chazot, G., Bourdon, E., Cotten, J., 2010. Evolving metasomatic agent in the Northern Andean subduction zone, deduced from magma composition of the long-lived Pichincha volcanic complex (Ecuador). Contrib Mineral Petrol 160, 239–260. https://doi.org/10.1007/s00410-009-0475-5

Schiano, P., Monzier, M., Eissen, J.-P., Martin, H., Koga, K.T., 2010. Simple mixing as the major control of the evolution of volcanic suites in the Ecuadorian Andes. Contrib Mineral Petrol 160, 297–312. https://doi.org/10.1007/s00410-009-0478-2

Shackleton, N.J., Sánchez-Goñi, M.F., Pailler, D., Lancelot, Y., 2003. Marine Isotope Substage 5e and the Eemian Interglacial. Global and Planetary Change, THE EEMIAN INTERGLACIAL: A GLOBAL PERSPECTIVE 36, 151–155. https://doi.org/10.1016/S0921-8181(02)00181-9

Sierra, D., Hidalgo, S., Almeida, M., Vigide, N., Lamberti, M.C., Proaño, A., Narváez, D.F., 2020. Temporal and spatial variations of CO2 diffuse volcanic degassing on Cuicocha Caldera Lake – Ecuador. Journal of Volcanology and Geothermal Research 107145. https://doi.org/10.1016/j.jvolgeores.2020.107145

Singer, B.S., Wijbrans, J.R., Nelson, S.T., Pringle, M.S., Feeley, T.C., Dungan, M.A., 1998. Inherited argon in a Pleistocene andesite lava: 40Ar/39Ar incremental-heating and laser-fusion analyses of plagioclase. Geology 26, 427–430. https://doi.org/10.1130/0091-7613(1998)026<0427:IAIAPA>2.3.CO;2

Soulas, J.-P., Eguez, A., Yepes, Hugo, Perez, H., 1991. Tectónica activa y riesgo sísmico en los Andes Ecuatorianos y el extremo sur de Colombia. Bol. Geol. Ecuat. 2, 3–11.

Spikings, R., Winkler, W., Hughes, R.A., Handler, R., 2005. Thermochronology of allochthonous terranes in Ecuador: Unravelling the accretionary and post-accretionary history of the Northern Andes. Tectonophysics, Andean Geodynamics: 399, 195–220. https://doi.org/10.1016/j.tecto.2004.12.023

Steiger, R.H., Jäger, E., 1977. Subcommission on geochronology: Convention on the use of decay constants in geo- and cosmochronology. Earth and Planetary Science Letters 36, 359–362. https://doi.org/10.1016/0012-821X(77)90060-7

Sun, S.-S., McDonough, W.F., 1989. Chemical and isotopic systematics of oceanic basalts: implications for mantle composition and processes. Geol. Soc. Lond. Spec. Publ. 42, 313–345. https://doi.org/10.1144/GSL.SP.1989.042.01.19

Thouret, J.-C., Finizola, A., Fornari, M., Legeley-Padovani, A., Suni, J., Frechen, M., 2001. Geology of El Misti volcano near the city of Arequipa, Peru. GSA Bulletin 113, 1593–1610. https://doi.org/10.1130/0016-7606(2001)113<1593:GOEMVN>2.0.CO;2

Tibaldi, A., Ferrari, L., 1992. From latest miocene thrusting to quaternary transpression and transtension in the Interandean Valley, Ecuador. Journal of Geodynamics 15, 59–83. https://doi.org/10.1016/0264-3707(92)90006-E

Vallejo, C., 2007. Evolution of the Western Cordillera in the Andes of Ecuador (Late Cretaceous-Paleogene) (Ph.D. thesis). University of Aberdeen, Zürich.

Vallejo, C., Almagor, S., Romero, C., Herrera, J.L., Escobar, V., Spikings, R., Winkler, W., Vermeesch, P., 2020. Sedimentology, Provenance and Radiometric Dating of the Silante Formation: Implications for the Cenozoic Evolution of the Western Andes of Ecuador. Minerals 10, 929. https://doi.org/10.3390/min10100929

Vallejo, C., Spikings, R., Horton, B.K., Luzieux, L., Romero, C., Winkler, W., Thomsen, T.B., 2019. Chapter 8 - Late cretaceous to miocene stratigraphy and provenance of the coastal forearc and Western Cordillera of Ecuador: Evidence for accretion of a single oceanic plateau fragment, in: Horton, B.K., Folguera, A. (Eds.), Andean Tectonics. Elsevier, pp. 209–236. https://doi.org/10.1016/B978-0-12-816009-1.00010-1

Vallejo, C., Winkler, W., Spikings, R., Luzieux, L., Heller, F., Bussy, F., 2009. Mode and timing of terrane accretion in the forearc of the Andes in Ecuador. Geological Society of America Memoirs 204, 197–216. https://doi.org/10.1130/2009.1204(09)

Voight, B., Komorowski, J.-C., Norton, G.E., Belousov, A.B., Belousova, M., Boudon, G., Francis, P.W., Franz, W., Heinrich, P., Sparks, R.S.J., Young, S.R., 2002. The 26 December (Boxing Day) 1997 sector collapse and debris avalanche at Soufrière Hills Volcano, Montserrat. Geological Society, London, Memoirs 21, 363–407. https://doi.org/10.1144/GSL.MEM.2002.021.01.17

von Hillebrandt, C., 1989. Estudio geovolcanológico del complejo volcánico Cuicocha-Cotacachi y sus aplicaciones, Provincia de Imbabura (Master’s thesis). Escuela Politécnica Nacional, Quito, Ecuador.

Winkler, W., Villagómez, D., Spikings, R., Abegglen, P., Tobler, St., Egüez, A., 2005. The Chota basin and its significance for the inception and tectonic setting of the inter-Andean depression in Ecuador. Journal of South American Earth Sciences, Cenozoic Andean Basin Evolution 19, 5–19. https://doi.org/10.1016/j.jsames.2004.06.006

Witt, C., Bourgois, J., Michaud, F., Ordoñez, M., Jiménez, N., Sosson, M., 2006. Development of the Gulf of Guayaquil (Ecuador) during the Quaternary as an effect of the North Andean block tectonic escape. Tectonics 25. https://doi.org/10.1029/2004TC001723

FIGURES

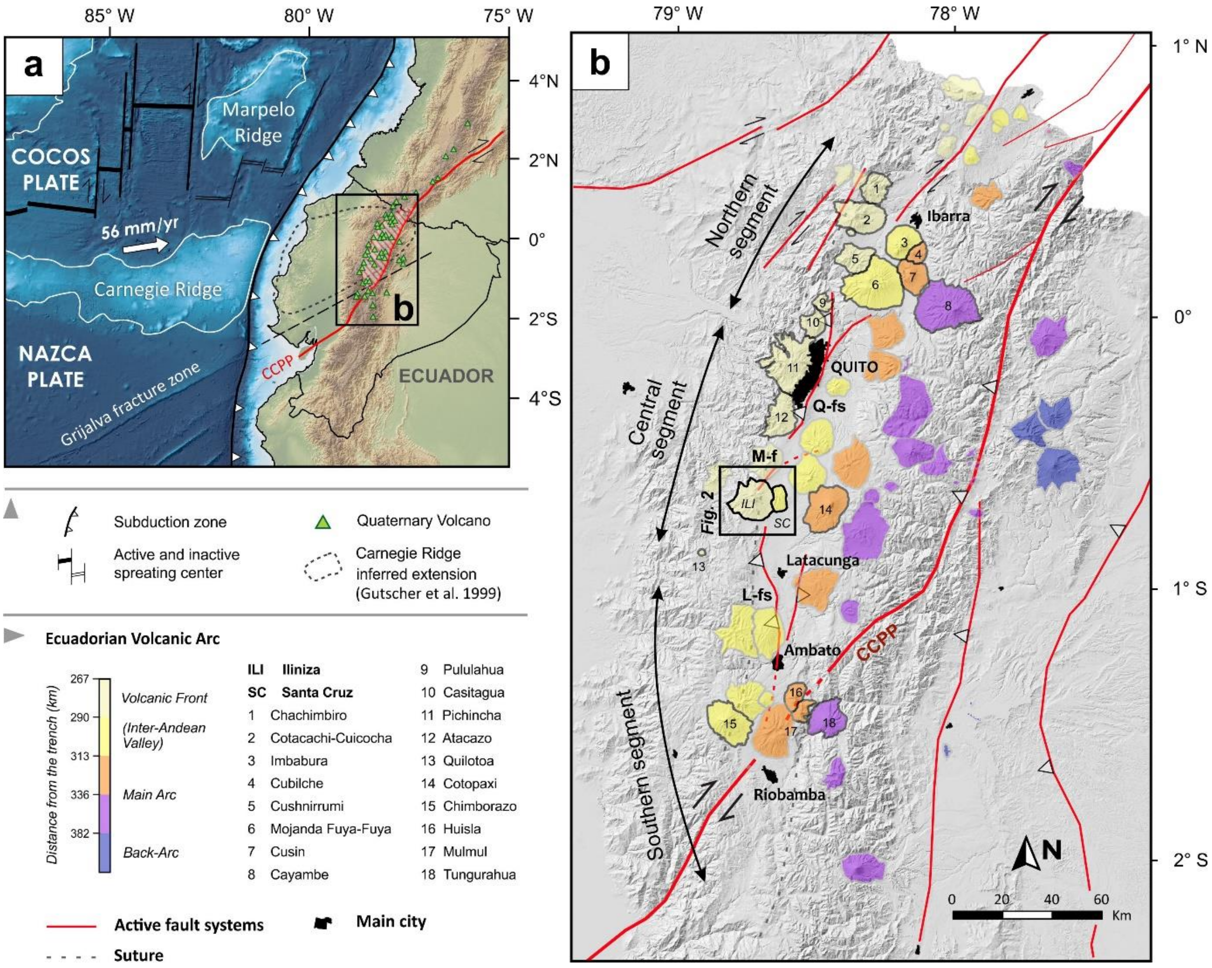

Figure 1. a) Geodynamic setting of the Ecuadorian arc (Modified from Gutscher et al., 1999). Arrows indicate the direction of the Nazca plate motion relative to the South American continental margin according to DeMets et al. (2010). **b)** Schematic map of the Ecuadorian volcanic arc. Volcanoes are colored according to their distance from the trench comprising the N-S alignments of the Volcanic Front (Western Cordillera), Inter-Andean Valley, Main Arc (Eastern Cordillera), and Back-Arc. Variability in the number of volcanic centers is represented by the northern, central, and southern across-arc segments. Iliniza (ILI) and Santa Cruz (SC) volcanoes, as well as those mentioned in the text, are outlined with black and grey borders, respectively. Active fault systems are represented with red lines according to Alvarado et al. (2016). CCPP: Chingual-Cosanga-Pallatanga-Puná Fault System; Q-fs: Quito Fault System; M-f: Machachi Fault; L-fs: Latacunga Fault System.

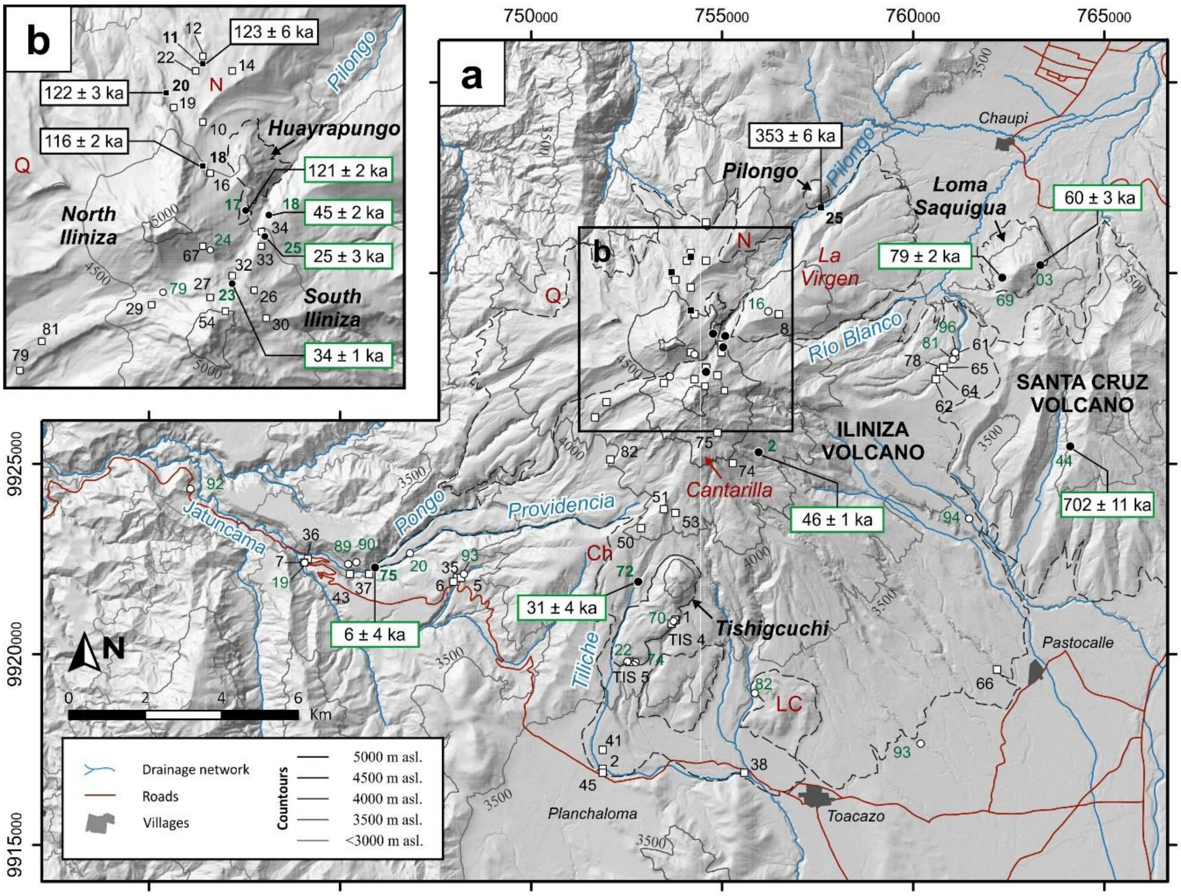

Figure 2. Hill-shaded digital surface model of Iliniza volcano showing the locations of new samples (circles; green numbers) and those from Hidalgo et al. (2007) (squares; black numbers). K-Ar dated samples are represented with solid symbols. Volcanic peaks shown as black letters. Ridges and hills shown as red letters. Ch: Chilcapamba; LC: Loma La Cruz; N: Ninarrumi; Q: Quillotoro. Rivers and valleys are labelled with blue letters.

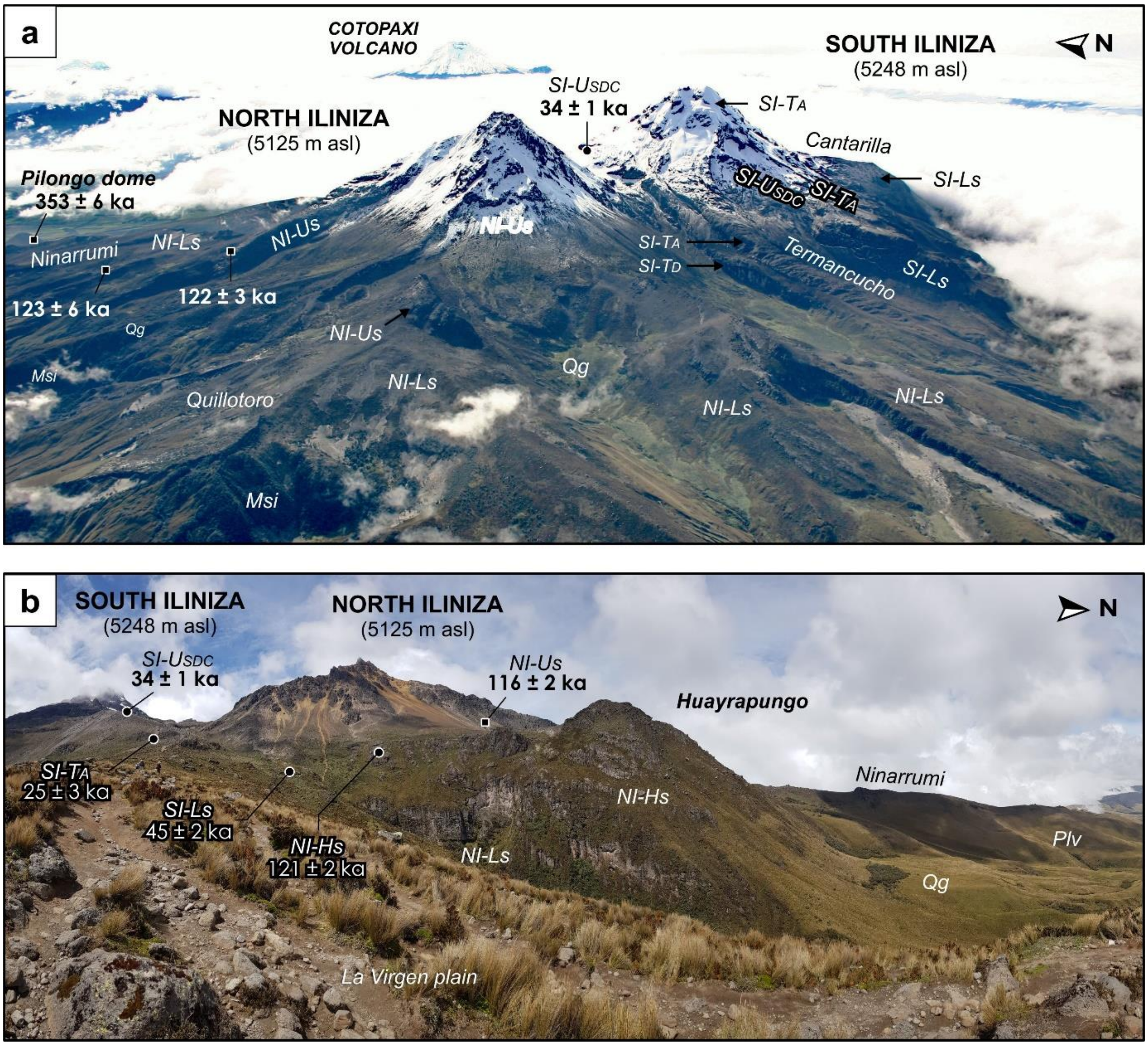

Figure 3. a) Aerial view of Iliniza volcano, looking east (photography by Patricio Ramon, IG-EPN). **b)** Panoramic view of the North Iliniza edifice, looking west from La Virgen plain. Geological unit abbreviations as in Figure 4.

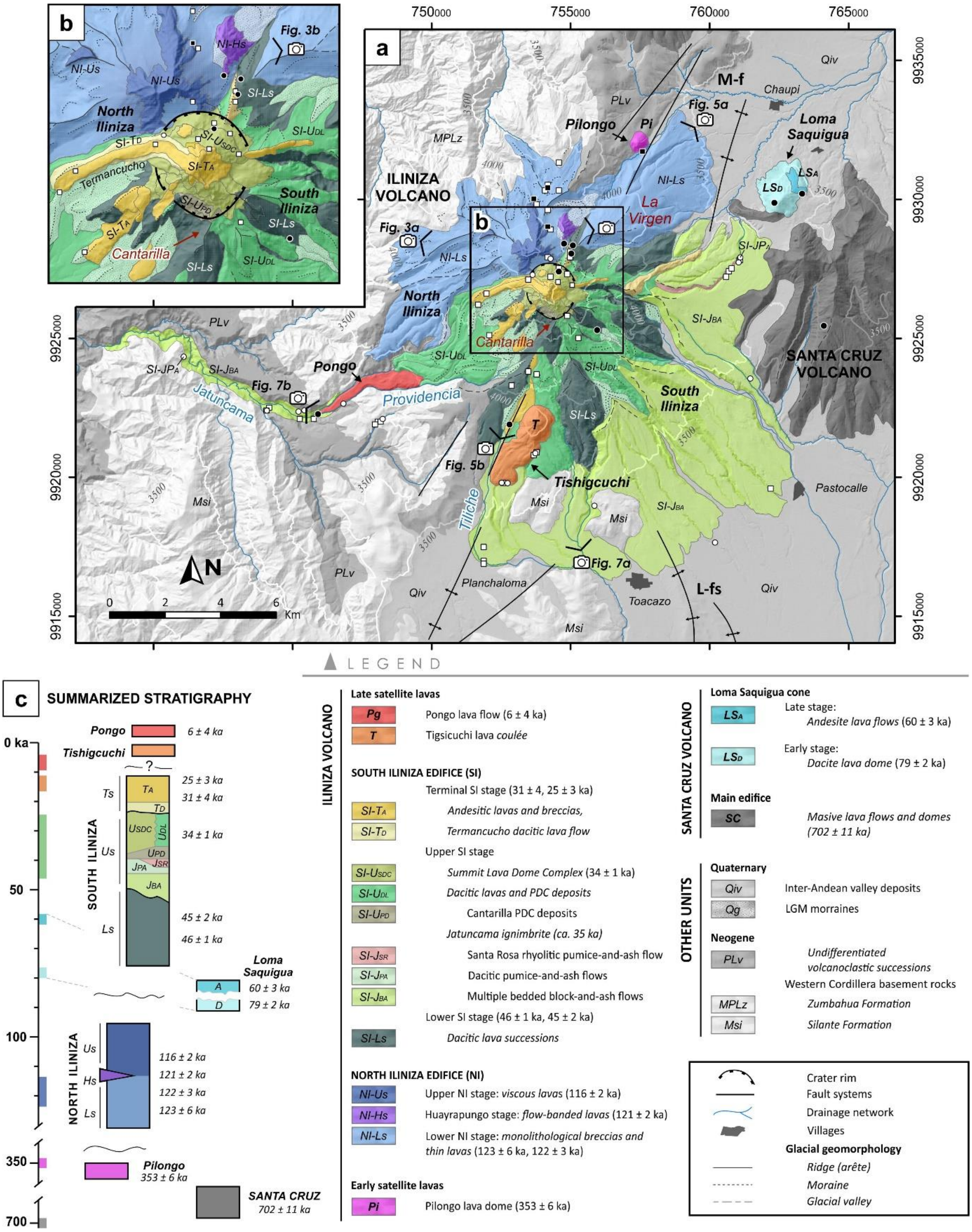

Figure 4. Simplified geological map of Iliniza volcano after considering our new ages (Table 1) and field observations, as well as those from Hidalgo (2001) and Hidalgo et al. (2007). Sample sites are shown according to figure 2 caption. Local fault systems are symbolized with black lines. M-f: Machachi Fault; L-fs: northern segment of Latacunga Fault System.

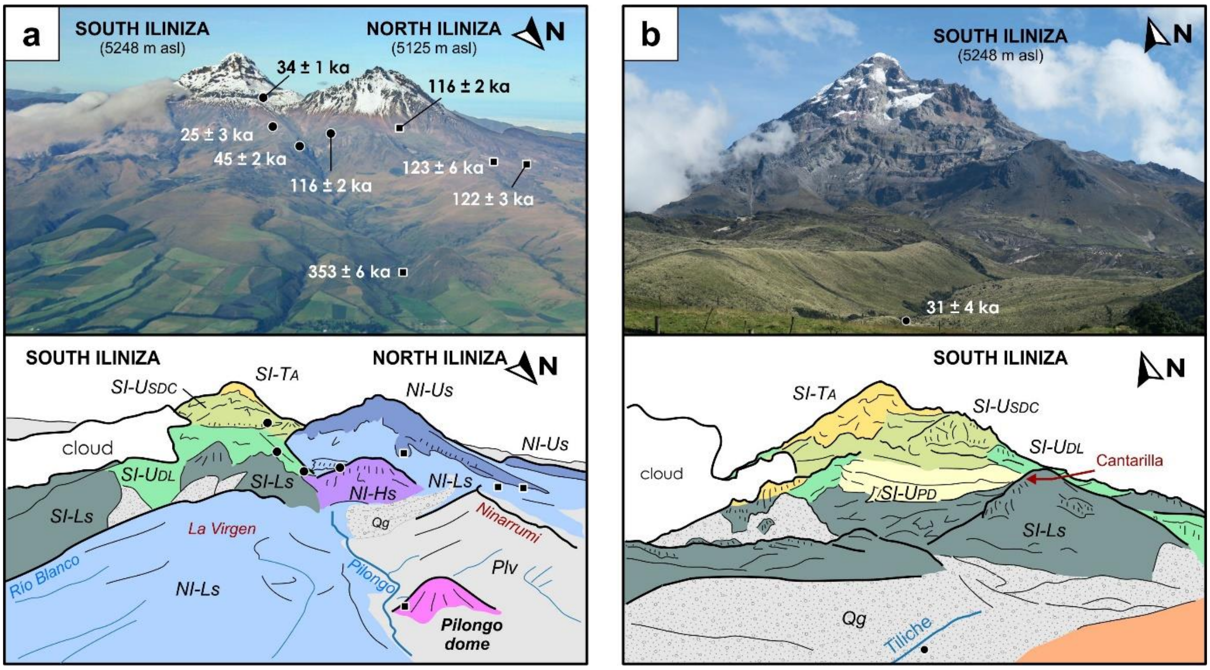

Figure 5. View of **a)** Iliniza volcano, looking south (photography by Patricio Ramon, IG-EPN), and **b)** South Iliniza edifice, looking north, showing the relationships between the main stratigraphic units represented according to Figure 4.

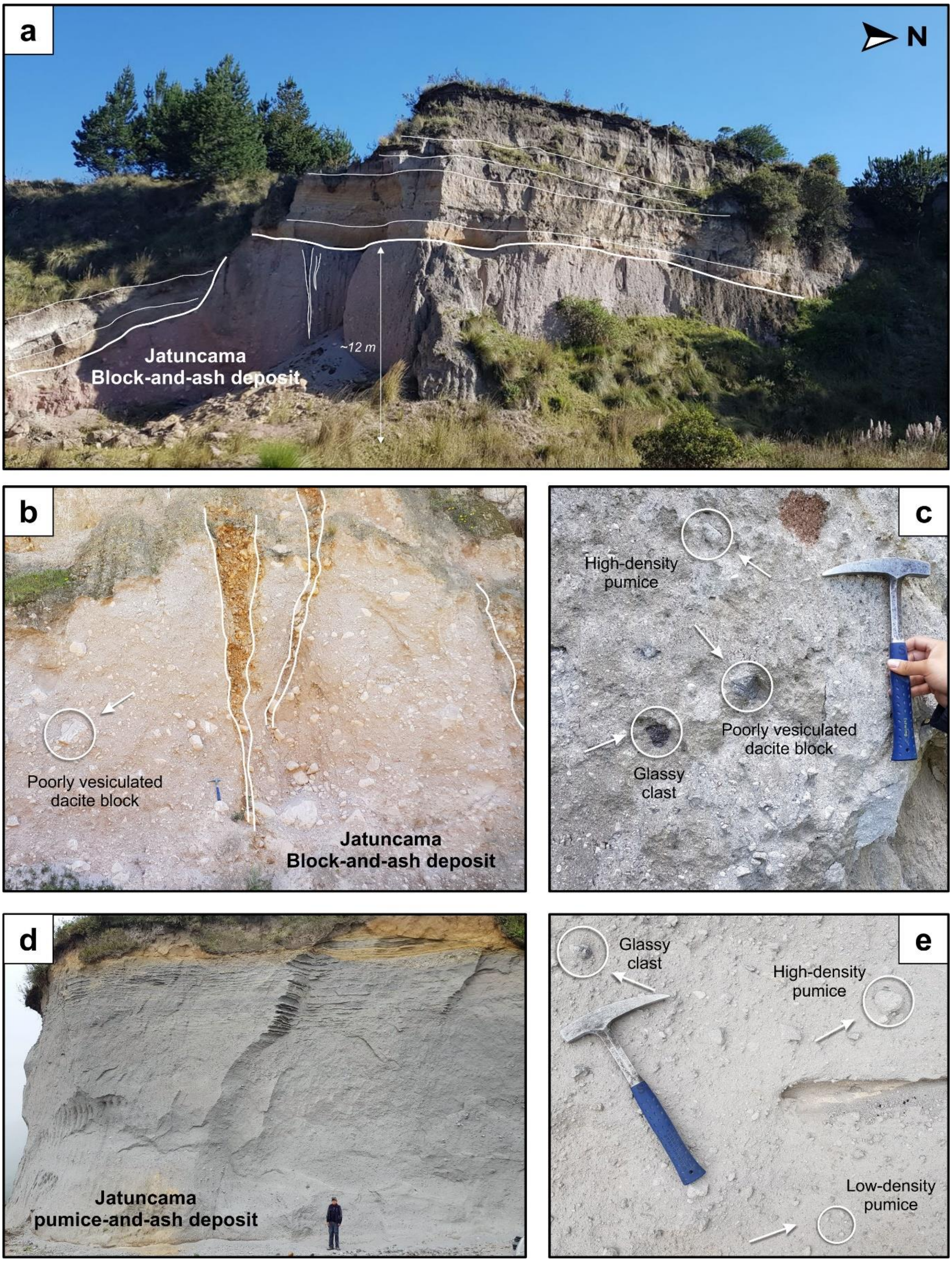

Figure 6. a) Jatuncama ignimbrite deposit at Planchaloma (site ILI 2), and **b)** detailed view of its degassing pipes structures. The deposit is discordantly overlain by lahars, Cotopaxi tephra fallouts, and soils. **c)** Types of clasts observed in a lower section of the ignimbrite deposit at

the Jatuncama valley (site 19EQ19). **d)** Pumice-and-ash flow observed at Jatuncama valley (site 20EQ92), and **e)** detailed view of its clastic components.

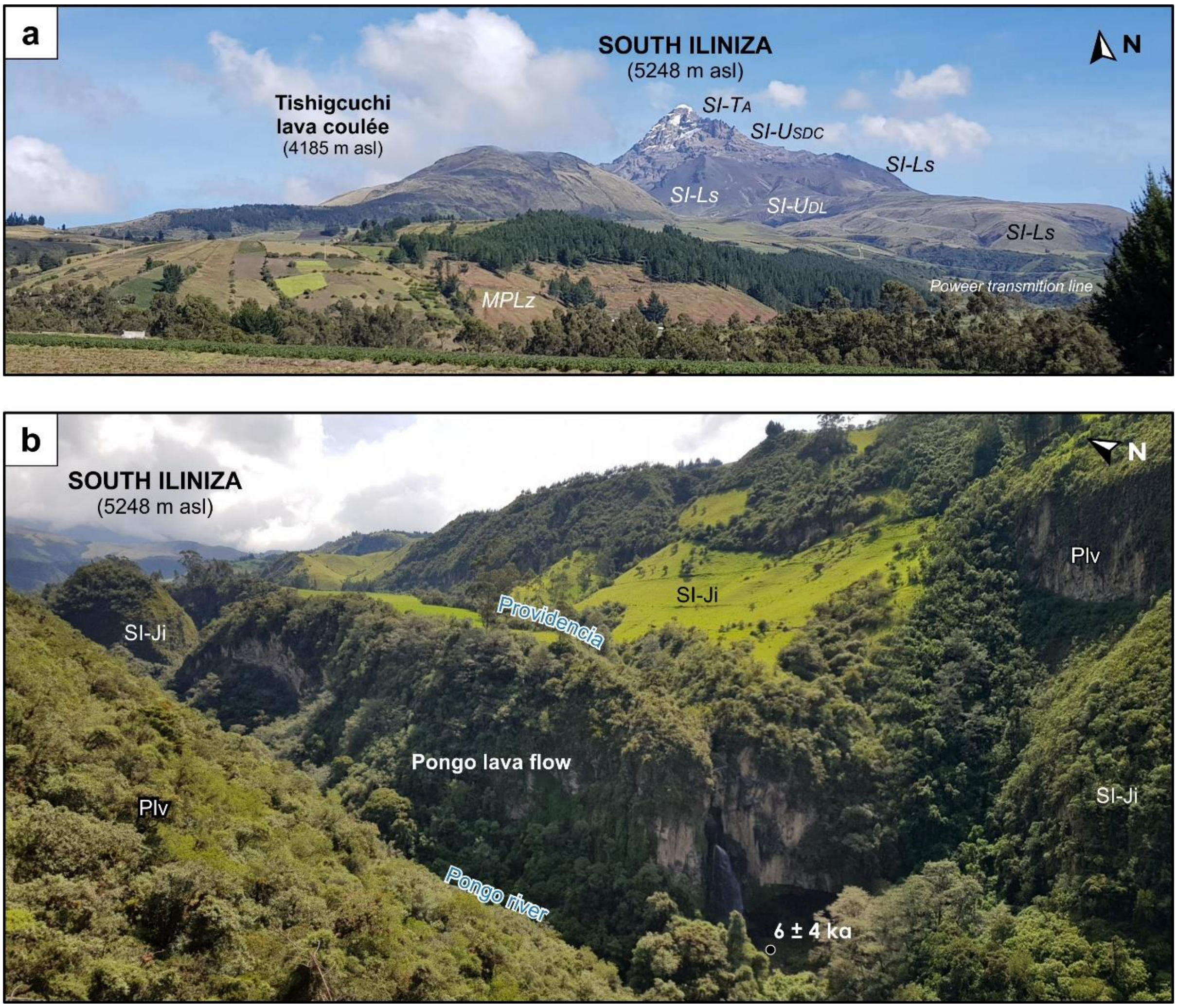

Figure 7. a) Panoramic view of the Tishigcuchi lava dome and the South Iliniza, looking north. **b)** View of the Pongo lava flow from the Jatuncama valley. Volcanological unit abbreviations as in Figure 4.

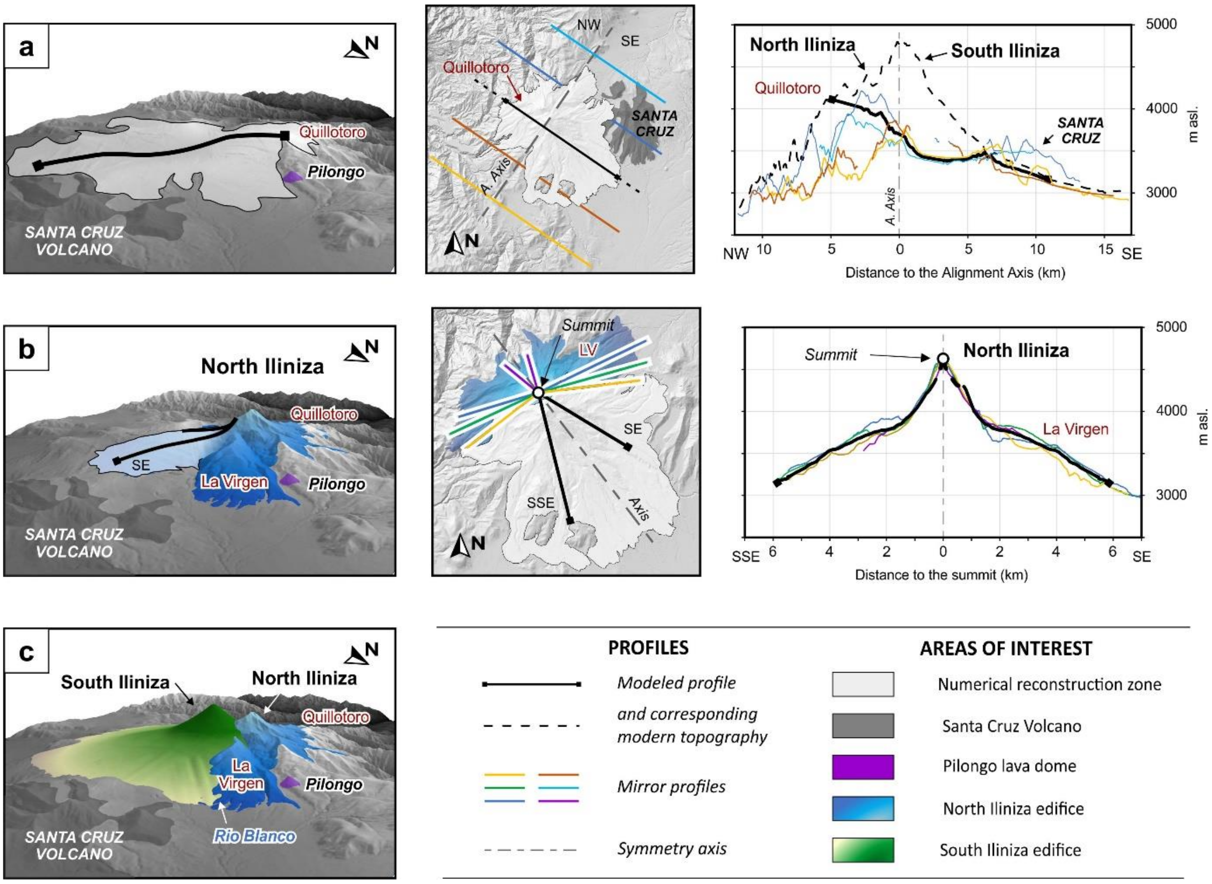

Figure 8. Model topographic profiles used for the reconstruction of the basement surface area of **a)** North Iliniza and **b)** South Iliniza edifices. Figures correspond, from left to right, to perspective and plan views of the reconstructed area, and to the mirror profiles used to create the modeled profile. **c)** Aerial view of the South Iliniza modeled cone fitted next to the partially eroded North Iliniza edifice.

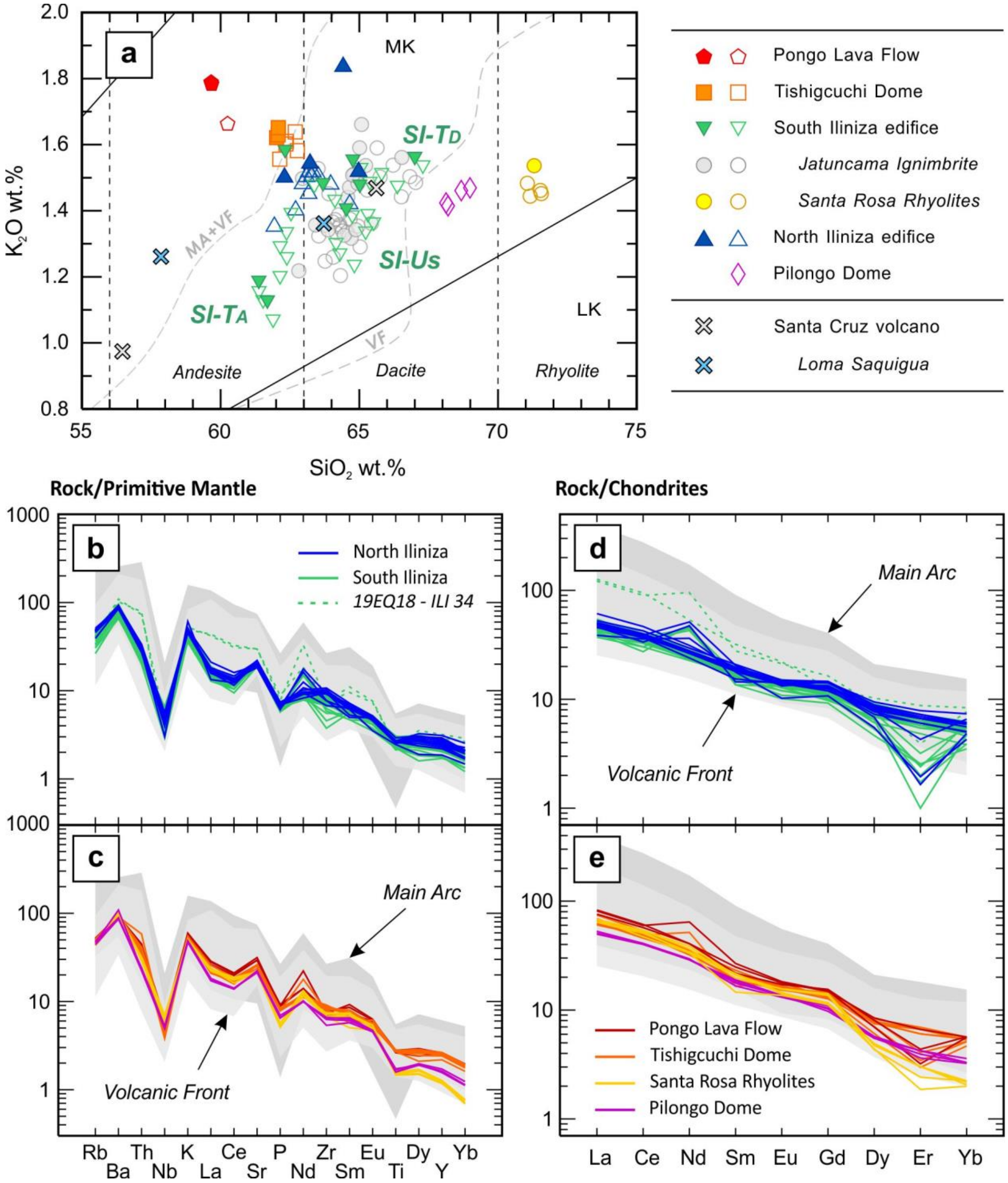

Figure 9. a) K_2O vs SiO_2 diagram (Peccerillo and Taylor, 1976) for eruptive products of Iliniza and Santa Cruz volcanoes. MK: medium-K, and LK: low-K calc-alkaline series. The late evolutionary stages of the South Iliniza edifice are shown with green symbols. Volcanological unit abbreviations as in Figure 4. Gray dashed lines indicate the composition fields created by the Volcanic Front (VF) and Main Arc (MA) whole-rock data obtained from the Georoc database. Open symbols are for data from Hidalgo et al. (2007). **b-c)** Incompatible trace elements normalized to primitive mantle spider diagrams (Sun and McDonough, 1989) for

North and South Iliniza edifices, and Iliniza satellite lavas and the SI-J$_{SR}$ units, respectively. **d-e)** Rare Earth Elements normalized to chondrites diagram (Sun and McDonough, 1989) for the same arrangements. Dark grey and light grey areas represent the composition fields depicted by the Volcanic Front and Main Arc whole-rock data (Georoc database), respectively.

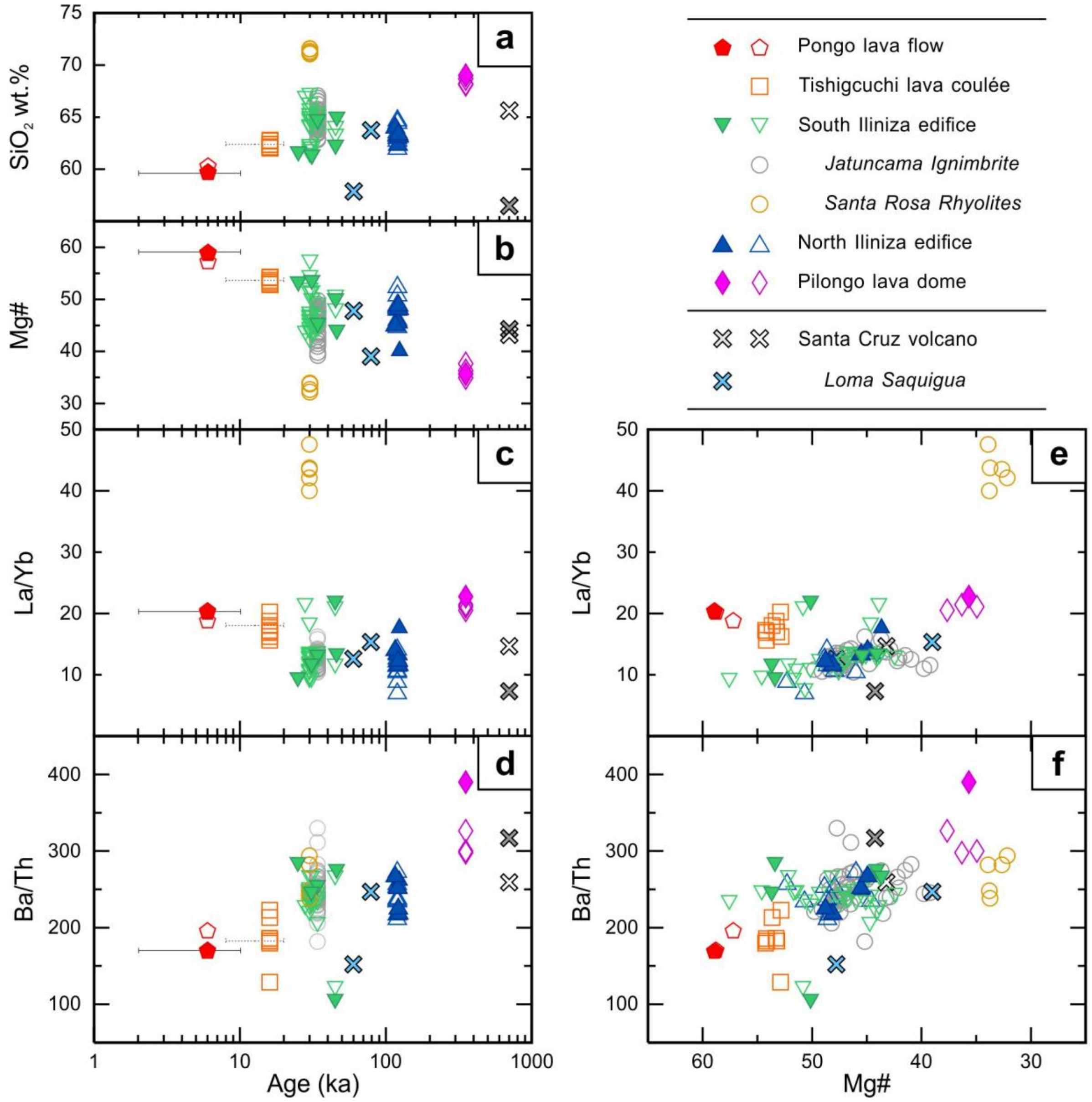

Figure 10. Temporal variations of **a)** Mg# (=100∗Mg/(Mg+Fe^{2+})), **b)** SiO$_2$ (wt.%), and **c)** La/Yb and **d)** Ba/Th ratios. Horizontal axis represents the timeline (ka) in logarithmic scale. **e)** La/Yb and **f)** Ba/Th ratios plotted against Mg#. Filled symbols are for dated samples (Table 1). The 1σ age uncertainty is shown with a solid line for Pongo lava flow, while the age estimation range is shown as a dashed line for Tishigcuchi lava coulée.

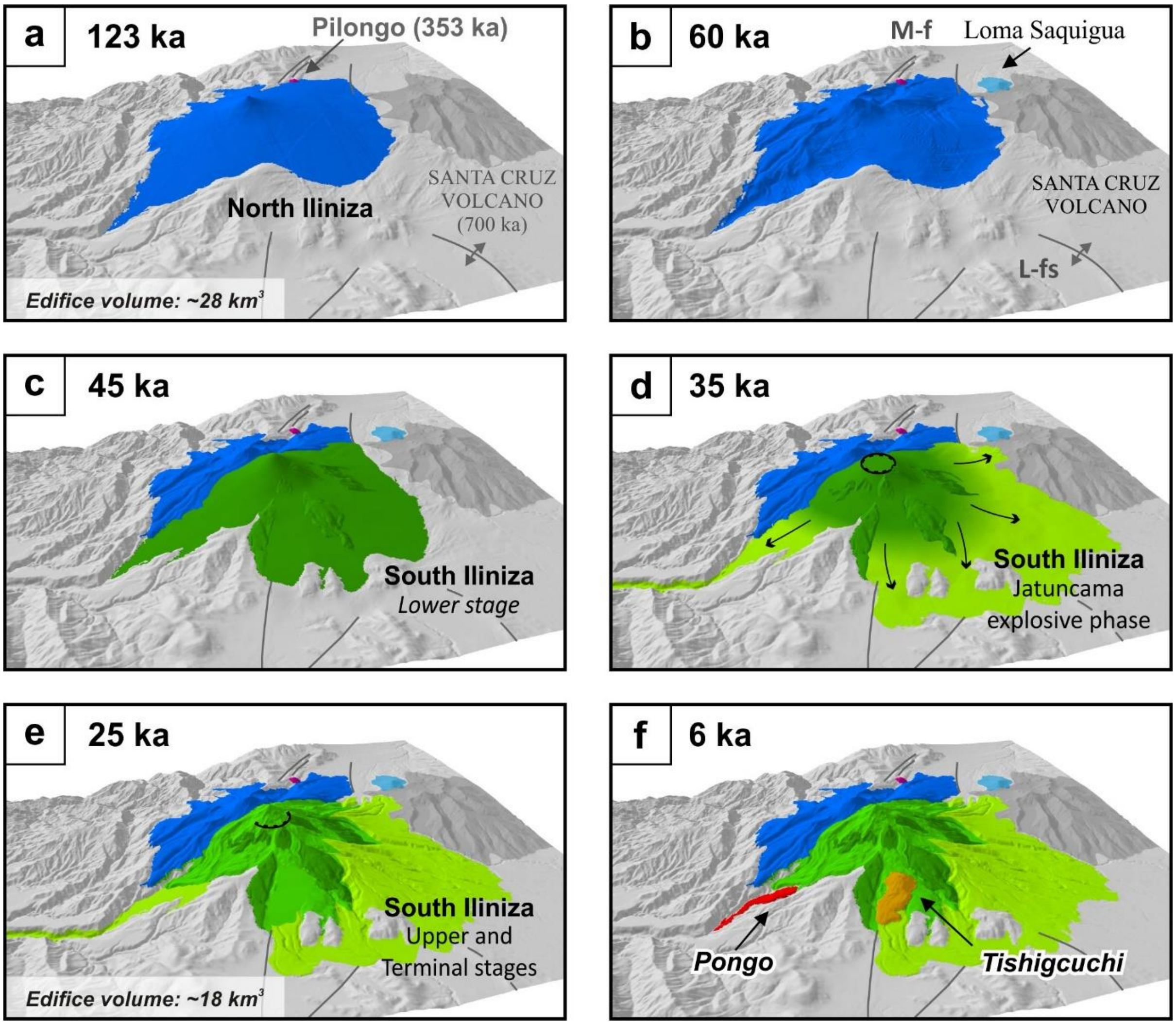

Figure 11. Synthetic charts showing the evolution of Iliniza and Santa Cruz volcanoes through time based on our numerical reconstructions. **a)** North Iliniza edifice construction; **b)** Santa Cruz volcano reactivation with the Loma Saquigua lavas emission; **c)** South Iliniza Lower Cone construction; **d)** the Jatuncama highly explosive eruptive phase creating a thick pyroclastic deposit; **e)** South Iliniza Upper cone construction and terminal lavas emission; and **f)** Holocene Tishigcuchi lava coulée and Pongo lava flow. Note that illustrations of phases c and d are mostly schematic, see text for details. Local fault systems are symbolized with black lines. M-f: Machachi Fault; L-fs: northern segment of Latacunga Fault System

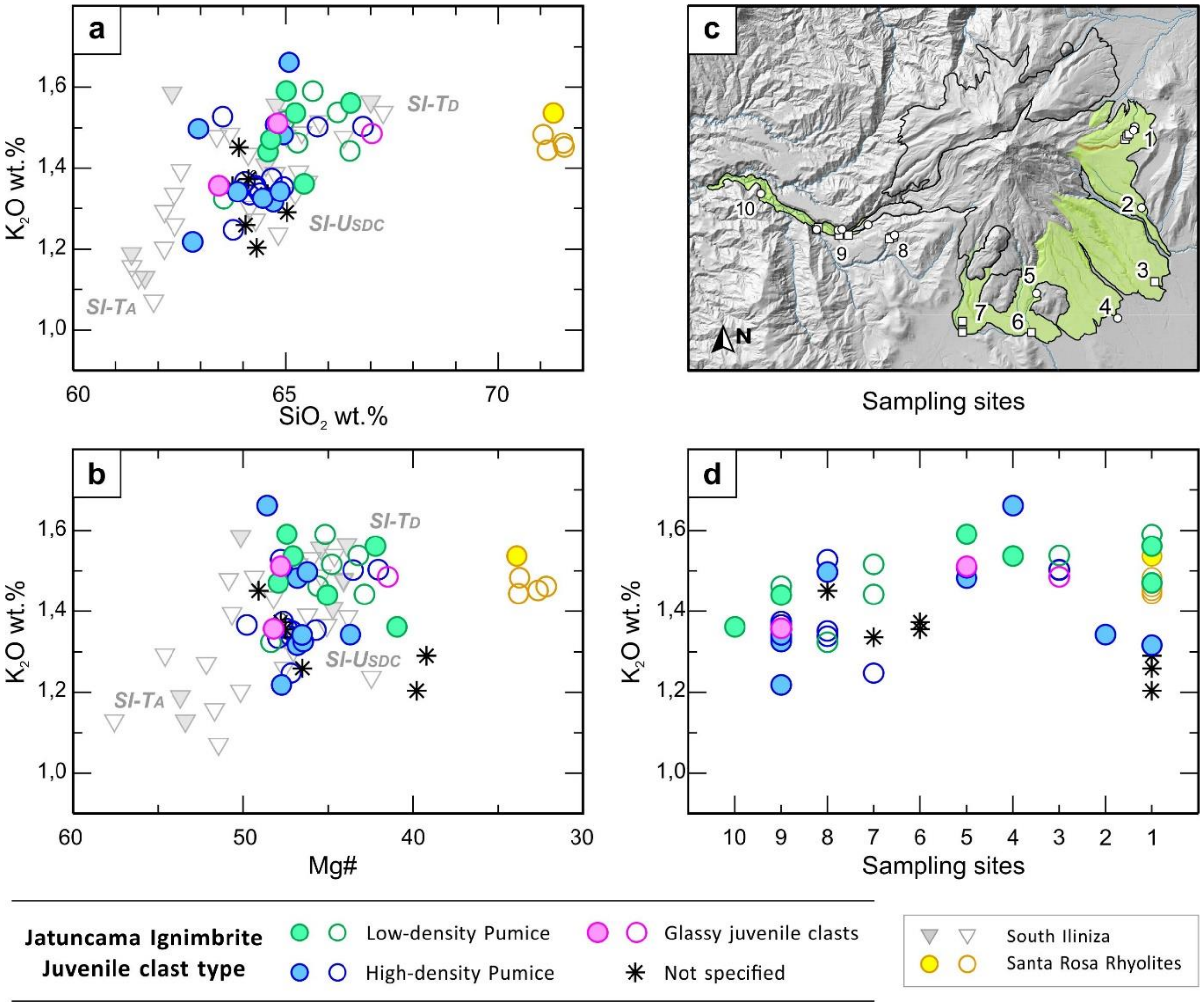

Figure 12. Geochemical diagrams for Jatuncama pyroclastic samples classified by clast type. K_2O versus **a)** SiO_2 and **b)** Mg# (=100∗Mg/(Mg+Fe^{2+})) diagrams. SI-U_{SDC}: South Iliniza upper cone; SI-T_D: Dacite Terminal Lavas; SI-T_A: Andesite Terminal Lavas. **C)** Geographical distribution of sampling sites around the base of South Iliniza and **d)** their variation in K_2O content. Open symbols are for data from Hidalgo et al. (2007).

TABLES

Table 1. (caption provided bellow the table)

Sample	Location and Unit	Longitude (m)	Latitude (m)	K (%)	^{40}Ar* (%)	^{40}Ar* (10^{11} at/g)	Age ± 1σ (ka)	Mean age (ka)
ILINIZA VOLCANO								
Pilongo lava dome								
ILI 25	Lava dome, Pilongo valley	757550	9931731	1.641	10.0%	6.0596	354 ± 6	**353 ± 6**
					16.4%	6.0422	352 ± 5	
North Iliniza edifice								
ILI 11	Monolithological breccia, N flank, *NI-Ls*	754150	9930434	2.404	2.0%	3.0594	122 ± 6	**123 ± 6**
					2.1%	3.1022	124 ± 6	
ILI 20	Monolithological breccia, N flank, *NI-Ls*	753648	9930031	2.148	5.5%	2.7666	123 ± 3	**122 ± 3**
					5.0%	2.6825	120 ± 3	
19EQ17	Lava flow, Huayrapungo peak, *NI-Hs*	754734	9928425	2.226	7.3%	2.8472	122 ± 2	**121 ± 2**
					6.8%	2.7715	119 ± 2	
ILI 18	Lava flow, N flank, *NI-Us*	754151	9929036	1.878	8.6%	2.2906	117 ± 2	**116 ± 2**
					8.7%	2.2671	116 ± 2	
South Iliniza edifice								
19EQ02	Lava flow, E flank, *SI-Ls*	755922	9925321	1.728	3.7%	0.8557	47 ± 1	**46 ± 1**
					3.1%	0.8006	44 ± 2	
19EQ18	Lava flow, N flank, *SI-Ls*	755052	9928362	1.667	1.9%	0.7908	45 ± 2	**45 ± 2**
					1.9%	0.7826	45 ± 2	
19EQ23b	Lava dome, summit area, $SI\text{-}U_{SDC}$	754550	9927424	2.302	3.1%	0.8144	34 ± 1	**34 ± 1**
					3.1%	0.8078	34 ± 1	
20EQ72	Lava flow, S flank (Tiliche river), $SI\text{-}T_{A}$	752778	9921934	1.206	0.8%	0.3788	30 ± 4	**31 ± 4**
					0.9%	0.3921	31 ± 4	
19EQ25	Monolithological breccia, N flank, $SI\text{-}T_{A}$	754997	9928069	1.311	0.9%	0.3273	24 ± 3	**25 ± 3**
					0.9%	0.3631	27 ± 3	
Pongo lava flow								
20EQ75	Lava flow, Pongo valley	745904	9922305	1.534	0.2%	0.0922	6 ± 4	**6 ± 4**
					0.2%	0.1017	6 ± 4	
SANTA CRUZ VOLCANO								
19EQ44	Lava flow, S flank, *SC*	764061	9925476	1.096	14.7%	7.9746	697 ± 11	**702 ± 11**
					15.4%	8.0858	706 ± 11	
Loma Saquigua								
20EQ69	Lava dome, *LS-d*	762285	9929891	1.480	5.8%	1.2233	79 ± 2	**79 ± 2**
					6.8%	1.2283	79 ± 2	
19EQ03	Lava flow, N flank, *LS-a*	763281	9930218	1.417	1.8%	0.8927	60 ± 3	**60 ± 3**
					2.2%	0.8868	60 ± 3	

Table 1. K-Ar ages obtained in this study for Iliniza and Santa Cruz volcanoes listed in decreasing order from oldest to youngest. Column headings indicate sample name, outcrop and relative location, volcanological unit (abbreviations as in Figure 4), sample coordinates, potassium (K) content in percent, radiogenic argon content (^{40}Ar*) in percent and in 10^{11} atoms per gram, age obtained for each measurement, and weighted mean age in ka given with a 1-σ uncertainty.

Table 2. Generalized chronostratigraphy showing the main stages of the Iliniza volcano

Edifice	Cone-building stage/Unit		Age (ka)	Volcanology	Petrography
Late satellite lavas	Pongo lava flow		6 ± 4 ka	Effusive eruption: voluminous lava flow	Aphanitic andesite (59 wt.% SiO_2): pl, opx and cpx, ± pl
	Tishigcuchi lava dome		>20 and <8 ka	Lava dome-forming eruption	Andesite (62-63 wt.% SiO_2): pl, amp, opx, ± cpx
South Iliniza	Terminal stage		31 ± 4 to 25 ± 3 ka	Mainly effusive activity: voluminous lava flows and related pyroclastic deposits	Mostly andesites (61–63 wt.% SiO_2): pl, opx, cpx, ± amp
	Upper stage	Summit lava dome complex	34 ± 1 ka	Lava dome-forming eruptions and related PDC	Dacites (64–67 wt.% SiO_2): pl, amp, ± Fe–Ti oxides, ± cpx
		Jatuncama explosive phase	~35 ka	Explosive dome-forming eruption followed by a pumiceous phase: - Dacitic and rhyolitic pumice-and-ash flows - Multiple bedded block-and-ash flows	- Scarce rhyolites (71-72 wt.% SiO_2): pl, ± cpx (aegirine), ± Fe-Ti oxides - Dacites (63-67 wt.% SiO_2): pl, amp, ± cpx
	Cantarilla unconformity				
	Lower stage		45 ± 2 to 46 ± 1 ka	Mainly effusive activity: basal edifice construction	Dacites (62-65 wt. % SiO_2): pl, amp, cpx, ± opx, ± Fe-oxides
North Iliniza	Terminal stage		116 ± 2 ka	Mainly effusive activity: viscous lava flows	Acid-andesites to dacites (62-65 wt.% SiO_2): pl, cpx, opx, ± Fe-Ti oxides, ± amp
	Huayrapungo stage		121 ± 2 ka	Mainly effusive activity: voluminous flow-banded lava flow	Andesites (62 wt.% SiO_2): pl, opx, and scarce cpx, ± Fe-Ti oxides
	Lower stage		122 ± 6 to 123 ± 6 ka	Mainly effusive activity: thin lava flows	Acid-andesites to dacites (62-64 wt.% SiO_2): pl, opx, cpx, ± amp, ± Fe-Ti oxides
Early satellite lavas	Pilongo lava dome		353 ± 6 ka	Lava dome-forming eruption	Porphyritic rhyodacite (68-69 wt.% SiO_2): pl, amp, opx, ± cpx, ± Fe-Ti oxides

Abbreviations: pl=plagioclase, amp=amphibole, cpx =clinopyroxene, opx=orthopyroxene.

Table 3. Construction and erosion volumes calculated based on numerical reconstructions together with their corresponding rates. Numerical results given with a 1-σ uncertainty (see text for details).

Unit	Volume (km^3)	Period (ka)	Duration (kyr)	Output rate (km^3 kyr^{-1})	Volume (km^3)	Period (ka)	Duration (kyr)	Erosion rate (km^3 kyr^{-1})
ILINIZA VOLCANO								
Main edifices								
North Iliniza	28 ± 9	124 - 116	8 ± 5	**3.5 ± 2.6**	6 ± 2			
Western flank					3 ± 1	116 - 0	116 ± 2	**0.03 ± 0.01**
South Iliniza	18 ± 6	46 - 25	21 ± 4	**0.8 ± 0.3**	6 ± 2	25 - 0	25 ± 3	**0.24 ± 0.09**
Satellite Vents								
Pilongo lava dome	$18 \pm 5 \times 10^{-3}$							
Tishigcuchi lava dome	$339 \pm 41 \times 10^{-3}$							
Pongo lava flow	$73 \pm 18 \times 10^{-3}$							
Present-day whole volcano	34 ± 14	123 - 25	98 ± 7	**0.3 ± 0.1**				